
Electronic Thesis and Dissertation Repository

8-15-2013 12:00 AM

Numerical Simulation of an Open Channel Ultraviolet Waste-water Disinfection Reactor

Rajib Kumar Saha
The University of Western Ontario

Supervisor
Dr. Chao Zhang
The University of Western Ontario Joint Supervisor
Dr. Madhumita Ray
The University of Western Ontario

Graduate Program in Mechanical and Materials Engineering
A thesis submitted in partial fulfillment of the requirements for the degree in Master of Engineering Science
© Rajib Kumar Saha 2013

Follow this and additional works at: <https://ir.lib.uwo.ca/etd>



Part of the [Applied Mechanics Commons](#), and the [Computer-Aided Engineering and Design Commons](#)

Recommended Citation

Saha, Rajib Kumar, "Numerical Simulation of an Open Channel Ultraviolet Waste-water Disinfection Reactor" (2013). *Electronic Thesis and Dissertation Repository*. 1450.
<https://ir.lib.uwo.ca/etd/1450>

This Dissertation/Thesis is brought to you for free and open access by Scholarship@Western. It has been accepted for inclusion in Electronic Thesis and Dissertation Repository by an authorized administrator of Scholarship@Western. For more information, please contact wlsadmin@uwo.ca.

**NUMERICAL SIMULATION OF AN OPEN CHANNEL ULTRAVIOLET WASTE-
WATER DISINFECTION REACTOR**

(Thesis format: Monograph)

by

Rajib Kumar Saha

Graduate Program in Mechanical and Materials Engineering

A thesis submitted in partial fulfillment
of the requirements for the degree of
Master of Engineering Science

The School of Graduate and Postdoctoral Studies
The University of Western Ontario
London, Ontario, Canada

© Rajib Kumar Saha 2013

Abstract

The disinfection characteristics of an open channel ultra-violet (UV) wastewater disinfection reactor are investigated using a computational fluid dynamics (CFD) model. The model is based on the volume of fluid method to capture the water-air interface, the Lagrangian particle tracking method to determine the microbial particle trajectory and the discrete ordinate model to calculate the UV intensity field. The numerical predictions are compared with the available experimental data to validate the CFD model. A parametric study is performed to understand the effects of different parameters on the disinfection performance of the reactor. The hydraulic behaviour and the additive nature of disinfection for an open channel reactor with two lamp banks placed in series using different geometric configurations between the two lamp banks are also investigated. A scaling down methodology for the open channel reactor is developed and implemented in the CFD model to understand its applicability.

Keywords

CFD simulation, Open channel flow, UV disinfection, Wastewater treatment

Acknowledgments

I want to thank both of my supervisors for their continuous support and guidance. I would also like to thank Dr. Botao Peng from Trojan Technologies, Inc. London, ON, Canada for his help during the initial stage of this project. This research would have been impossible to finish without the computational resources provided by SHARCNET and the facilities at Western University. Support provided by the NSERC through the ENGAGE program is also acknowledged.

I want to thank my colleagues in the CFD lab at Western for maintaining a good work environment. Lastly and the most important of all, I want to thank my parents and family members for their continuous care and encouragement.

Table of Contents

| | |
|--|-----------|
| Abstract | ii |
| Acknowledgments..... | iii |
| Table of Contents | iv |
| List of Figures | vii |
| List of Tables | x |
| Nomenclature | xi |
| Chapter 1 | 1 |
| 1 Introduction | 1 |
| 1.1 UV Light and UV Lamp Types | 1 |
| 1.2 UV Reactor Configurations | 2 |
| 1.3 Reactor Performance Assessment and the Need for CFD | 3 |
| 1.4 Objectives of this Work | 5 |
| 1.5 Outline of the Thesis | 7 |
| Chapter 2 | 8 |
| 2 Literature Review | 8 |
| 2.1 Application of Different Computational Models in UV Reactor Simulations | 8 |
| 2.2 Application of Free Surface Tracking Schemes and Turbulence Models in Open Channel Flow Simulation | 16 |
| 2.3 Conclusion | 18 |
| Chapter 3 | 21 |
| 3 Description of the Numerical Model..... | 21 |
| 3.1 The Reactor Geometry | 21 |
| 3.2 Computational Model | 23 |
| 3.2.1 Turbulent Open Channel Flow with Water-air Interface | 23 |

| | | |
|------------------|---|-----------|
| 3.2.2 | Microbial Particle Trajectory | 27 |
| 3.2.3 | UV Intensity Field..... | 28 |
| 3.2.4 | Inactivation Kinetics | 31 |
| 3.3 | Boundary Conditions and Numerical Solution Techniques..... | 34 |
| 3.4 | Grid Generation | 37 |
| 3.5 | Scaling Down Methodology | 39 |
| 3.5.1 | Similarity of Hydraulics in Open Channel Flows..... | 39 |
| 3.5.2 | Similarity of the Radiation Field and the Disinfection Behaviour | 44 |
| Chapter 4 | | 47 |
| 4 | Results and Discussion..... | 47 |
| 4.1 | Grid Independence Test | 47 |
| 4.2 | CFD Model Validation | 50 |
| 4.3 | Effect of the Lamp Support Systems | 51 |
| 4.4 | Existence of Secondary Current in the Reactor | 53 |
| 4.5 | Parametric Analysis | 56 |
| 4.5.1 | Effect of the Flow Rate on the Free Surface Profile..... | 56 |
| 4.5.2 | Effect of Flow Rate and UV Sensitivity of the Microbes on the Disinfection Performance | 59 |
| 4.5.3 | Effect of the Water UVT on the Disinfection Performance | 61 |
| 4.6 | Visualization of the UV Radiation Intensity Distribution and Particle Doses..... | 63 |
| 4.7 | Reactors with Two Lamp Banks..... | 64 |
| 4.7.1 | Hydrodynamic Behaviour in the Reactor with Two Lamp Banks..... | 66 |
| 4.7.2 | Disinfection Behaviour in the Reactors with Two Lamp Banks | 71 |
| 4.8 | Scaled Down Reactor..... | 73 |
| 4.8.1 | Hydrodynamic Behaviour of the Scaled Down Reactor..... | 73 |
| 4.8.2 | Disinfection Behaviour of the Scaled Down Reactor | 75 |

| | |
|--|----|
| Chapter 5 | 77 |
| 5 Conclusions | 77 |
| References | 79 |
| Appendices | 85 |
| Appendix A - User Defined Function (UDF) | 85 |
| Curriculum Vitae | 87 |

List of Figures

| | |
|---|----|
| Figure 1.1: (a) Closed channel UV reactor (b) Open channel UV reactor | 3 |
| Figure 3.1: Schematic of the computational domain without lamp support system | 22 |
| Figure 3.2 Simplified lamp support system | 23 |
| Figure 3.3: Dose-response relationship for some microbes and their approximation to linear kinetics. | 32 |
| Figure 3.4: Boundary conditions for the momentum and continuity equations | 34 |
| Figure 3.5: Element distribution at a lateral cut-plane for the geometry without the lamp support system | 38 |
| Figure 3.6 The surface mesh on the lamp support and the volume mesh at a lateral-cut-plane. | 39 |
| Figure 4.1 Free surface profile for the reactor without the lamp support | 48 |
| Figure 4.2 Free surface for the reactor with the lamp support | 48 |
| Figure 4.3 Comparison of the predicted normalized water level using different grid sizes for the reactor without the lamp support | 49 |
| Figure 4.4 Comparison of the predicted normalized water level using different grid sizes for the reactor with the lamp support | 50 |
| Figure 4.5 Comparison of the predicted normalized free surface height with the experimental data. | 51 |
| Figure 4.6 Log removal of the microorganism for both of the reactor models with and without the lamp support system | 52 |
| Figure 4.7 Stream-wise velocity contour (m/s) at a horizontal plane passing through a lamp cross section. | 53 |

| | |
|--|----|
| Figure 4.8 Free surface height predicted by $k - \epsilon$ and RSM turbulence model | 54 |
| Figure 4.9 Iso-lines of stream-wise velocity magnitude at 0.5 m upstream of the lamp bank | 55 |
| Figure 4.10 Wall shear stress at 0.5m upstream of lamp bank | 56 |
| Figure 4.11 Comparison of the absolute free surface heights at different flow rates. | 58 |
| Figure 4.12 Comparison of the pressure head losses within the reactor at different flow rates. | 58 |
| Figure 4.13 Log removal and the obtainable RED at different flow rates..... | 60 |
| Figure 4.14 Probability density function of UV dose | 60 |
| Figure 4.15 Stream-wise velocity profile at the mid stream-wise cross section passing through the lamp | 61 |
| Figure 4.16 Variation of achievable log-removal with water UVT | 62 |
| Figure 4.17 UV intensity distribution around the lamps along a horizontal line for different UVT values. | 63 |
| Figure 4.18 Low dosed particle trajectories colored by the dose value (ranging from 0 to 30 mJ/cm^2)..... | 64 |
| Figure 4.19 Stream-wise velocity and turbulence intensity at mid-stream-wise plane | 66 |
| Figure 4.20 Free surface profile for the two-bank reactor having straight joint (colored with velocity magnitude m/s)..... | 67 |
| Figure 4.21 Free surface profile for the two-bank reactor having expanded joint (colored with velocity magnitude m/s)..... | 67 |
| Figure 4.22 Free surface profile for the two-bank reactor having constricted joint (colored with velocity magnitude m/s)..... | 68 |

| | |
|---|----|
| Figure 4.23 Comparison of the free surface heights for the two-bank reactors having different joints..... | 69 |
| Figure 4.24 Energy-depth curve | 71 |
| Figure 4.25 Reduction equivalent dose (RED) for the two-bank reactors compared with the one-bank reactor at 4320 gpm..... | 72 |
| Figure 4.26 Comparison of free surface profile for the full size and scaled down systems ... | 74 |
| Figure 4.27 Probability density of particle residence time at full size and scaled down models. | 74 |
| Figure 4.28 Comparison of the disinfection performance between the full size (4320 gpm) and scaled down models using only the Froude number and both Reynolds & Froude numbers..... | 76 |
| Figure 4.29 Probability density of dosage at the full size and scaled down reactors. | 76 |

List of Tables

Table 4.1 Additive behavior of RED in the reactors with two lamp banks 72

Nomenclature

| | | | |
|-------------------------------------|---|-------------------------|--|
| <i>a</i> | Absorption coefficient of the medium (m^{-1}) | <i>L</i> | Length scale (m) |
| <i>c</i> | UV sensitivity of the microbes ($\log J^{-1}m^2$) | <i>N, N₀</i> | Number of potent microbes after and before exposure to UV respectively |
| <i>c_{1, c₂}</i> | Model constants | <i>p</i> | Pressure (Pa) |
| <i>c_D</i> | Drag force coefficient of the particle | <i>p(D)</i> | Probability density of dose (-) |
| <i>d</i> | Diameter (m) | \vec{r} | Position vector |
| <i>D</i> | Dose ($J m^{-2}$) | <i>Re</i> | Relative Reynolds number |
| <i>d₁₀</i> | Required amount of dose for 1 log removal (Jm^{-2}/\log) | \vec{s} | Direction vector for the RTE |
| <i>Fr</i> | Froude number | \vec{s}' | The scattering direction vector |
| \vec{F} | Body force on fluid element (N) | <i>sc_s</i> | Scattering coefficient of the medium |
| \vec{g} | Gravitational acceleration vector ($m s^{-2}$) | <i>S</i> | Scalar measure of the deformation tensor |
| <i>G_k</i> | Production of turbulent kinetic energy due to the mean velocity gradients (m^2s^{-2}) | <i>t, T</i> | Time (s) |
| <i>I</i> | UV radiation intensity (Wm^{-2}) | \vec{v} | Velocity vector (m/s) |
| <i>k</i> | Turbulent kinetic energy (m^2s^{-2}) | <i>We</i> | Weber number |

Greek letters

| | | | |
|------------|---|-----------------------------|--|
| α | Volume fraction | $\sigma_k, \sigma_\epsilon$ | Turbulent Prandtl number for k and ϵ , respectively |
| ϵ | Turbulent kinetic energy dissipation rate (m^2s^{-3}) | $\bar{\sigma}$ | Fluid stress tensor |
| μ | Viscosity ($kg\ m^{-1}s^{-1}$) | $\bar{\tau}$ | Reynolds stress tensor |
| ρ | Density ($kg\ m^{-3}$) | | |

Subscripts

| | | | |
|---|--------------------------------|---|----------------------------------|
| m | Molecular | t | Turbulent |
| p | Particle | w | Water phase |
| r | Ratio (model to prototype) | x | x coordinate direction component |
| s | Scattering radiation component | | |

Abbreviations:

| | | | |
|------|-----------------------------------|-----|-----------------------------|
| CFD | Computational Fluid Dynamics | RNG | Renormalized group theory |
| DO | Discrete Ordinate | RSM | Reynolds stress model |
| DRW | Discrete random walk | RTE | Radiative Transfer Equation |
| LDA | Laser Doppler anemometry | RED | Reduction Equivalent Dose |
| LDV | Laser Doppler velocimetry | TKE | Turbulent kinetic energy |
| LSI | Line source integration | UV | Ultra-Violet |
| MPSS | Multiple points source summation | UVT | Ultraviolet Transmittance |
| MSSS | Multiple segment source summation | UDF | User Defined Functions |
| PDF | Probability Density Function | VOF | Volume of Fluid |
| PSS | Point source summation | | |

Chapter 1

1 Introduction

Ultraviolet (UV) light has been used extensively for disinfecting both drinking and waste-water containing microbial species. For waste-water disinfection, UV light is used at the tertiary stage of disinfection. In the primary and secondary stages of treatment, heavy solids and suspended biological components are removed using mainly mechanical processes. Unlike chlorination and ozonation which are commonly used during the tertiary stage of waste-water treatment, ultraviolet light is a green technology as no hazardous oxidation by-products are produced (Oppenheimer et al., 1997). It is also an effective disinfectant for some pathogens like spore forming *Cryptosporidium* and *Giardia lamblia*, which are relatively resistant to chemical disinfection (Linden et al., 2002).

The UV light disinfects the microorganism such as bacteria, viruses and pathogens by destroying their nucleic acid (DNA and RNA). This photochemical inactivation process is called dimerization. The UV light promotes a bond formation between nucleotides (thymine-thymine, thymine-cytosine, uracil-uracil and cytosine-cytosine) of two adjacent DNA/RNA strands. This bonding (dimer) prevents the organism from replicating or reproducing. As a result, they cannot infect their host.

1.1 UV Light and UV Lamp Types

In the electromagnetic radiation spectrum UV falls between X-rays and visible light (100 to 400 nm). According to the wavelength it can be classified to following categories:

- a) Vacuum UV (100 to 200 nm)
- b) UVC (200 to 280 nm)
- c) UVB (280 to 315 nm)
- d) UVA (315 to 400 nm)

In disinfection reactors the UV light is produced by the UV lamps. These lamps are composed of hermetically sealed silica or quartz bulb filled with an inert gas (argon) and

a small amount of mercury. The gas is excited with very high voltage difference between the tungsten electrodes. The mercury vapor at higher energy state caused by the arc comes to a low energy state and releases UV light. The wavelength of the emitted UV light depends on the gas pressure inside the lamp. The low pressure (0.93 Pa) lamp only emit light at certain wavelengths, usually 254 nm and 185 nm, (Wright and Cairns, 1998).

The UV absorption and consequently the microbial inactivation vary as a function of the wavelength of UV light. For most microorganisms, the UV absorption by the DNA is the maximum at or near 260 nm and drops to zero near 300 nm (USEPA, 2006). Since the 254 nm output of a low pressure lamp coincides well with this inactivation peak near 260 nm, the low pressure lamp is widely used in disinfections.

Medium pressure (13 kPa) lamps exhibit a continuous spectrum with several peaks. Mostly UVC and UVB are produced. Although in practical applications both the medium and low pressure lamps are used, the low pressure UV lamp is considered in this study.

1.2 UV Reactor Configurations

UV disinfection reactors can be classified as either closed or open channel. In open channel reactors there exists a free surface of the flowing fluid, i.e. the fluid is not entirely enclosed by solid boundaries. An example of these systems are shown in Figure 1.1. Closed channel reactors are mostly used for disinfecting drinking water. Open channel reactors have widespread use in disinfecting wastewater due to their high flow rate capability and low installation cost. In open channel reactors, UV lamps are directly placed within the water. The lamps are covered by a protective sleeve, which is usually made of quartz.

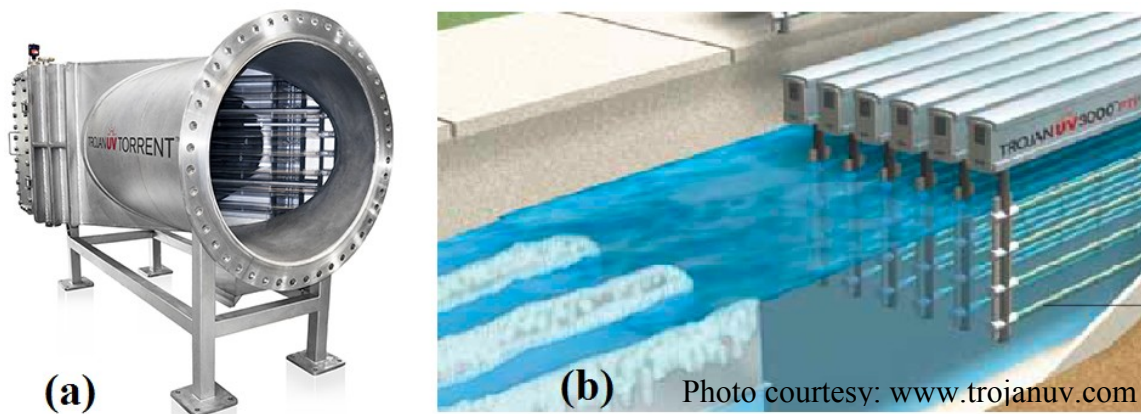


Figure 1.1: (a) Closed channel UV reactor (b) Open channel UV reactor

According to the arrangement of the UV lamps, open channel reactors are divided into two types: 1) horizontal configuration where the lamps are placed horizontally, parallel to the flow direction and 2) vertical configuration where the lamps are placed vertically, perpendicular to the flow. The lamp configuration in a reactor affects its disinfection performance. The horizontal configuration has a comparative advantage over the vertical one in terms of the distributed UV-radiation dose. Since the lamps are aligned with the stream-wise direction of the water flow, the exposure time of any microbial particle to the UV light is better in the reactor having horizontal arrangement of the lamps. In the vertical configuration, the lamps may be overheated at the top if the water surface falls below suddenly. This increases the risk of the lamp breakage due to the temperature variations. In addition, several studies were conducted on the open channel UV reactors with vertical configuration, whereas, no studies have been reported on the reactors with horizontal configuration. Therefore, the horizontal lamp configuration is considered in this study.

1.3 Reactor Performance Assessment and the Need for CFD

Before the UV disinfection reactor can be put to operation its inactivation performance should be evaluated. Quantification of the inactivation credit of a reactor is also important to improve the dose distribution and eventually minimize the energy consumption of the reactor.

Theoretically the plug flow reactors would provide the best disinfection performance. However, in reality the reactor dose delivery is not uniform. The geometric configuration of the reactor and the exponential decay of the UV intensity field due to absorption in radiation are responsible for the non-uniformity of the dose distribution. In open channel reactors, the waviness at the water-air interface is also responsible for this deviation.

The steps involved in the standard procedure for disinfection performance assessment of a UV reactor are explained in details in USEPA (2006) guideline. The widely used technique is bio-dosimetry, where the inactivation of the challenge microorganism is directly calculated by passing it through the reactor and sampling the inactivation at the outlet. This achieved inactivation is matched with the microorganism's dose response curve. Dose response curve quantifies the inactivation with response to dosage and is found from collimated beam experiments. From this curve the overall dose delivered by the reactor can be calculated from the achieved inactivation. However, if the challenge microorganism's dose-response behavior is not the same as those target organisms, this method cannot predict accurate disinfection behavior. Moreover, bio-dosimetry does not provide any information regarding the local disinfection behavior within the reactor.

If the dose distribution of the reactor could be directly measured by some means, the inactivation from the reactor for a microorganism having any dose-response curve could be easily evaluated. To achieve that purpose, different experimental techniques such as biological dosimeter (Cabaj and Sommer, 2000), Lagrangian actinometry (Bohrerova et al., 2005; Blatchley et al., 2006) and optical diagnostic techniques (Elyasi and Taghipour, 2011; Gandhi et al., 2012) have been developed. However, these experimental techniques require full size reactor model, which may not be cost effective for investigating multiple designs. One alternative approach is the use of numerical techniques to resolve the hydraulics and optics occurring inside the reactor and to calculate the dose distribution from that.

During the last two decades, computational fluid dynamics (CFD) simulation has been used by many researchers as it provides a cost effective approach to evaluate reactor performance or at least reduce the number of experimental approaches for possible design

modifications. Most of the computational studies performed to date on the UV disinfection reactors are restricted to closed channel configuration. However, the open channel configuration is widely used in wastewater treatment plants. Due to the complicated flow characteristics arising from the free surface in an open channel configuration, a comprehensive investigation is necessary. Literature provided a few instances of the simulation of the vertical type open channel reactors, whereas, none was found on the horizontal type. However, these works were based on different simplification, such as two-dimensional assumption and simplified turbulence models. These simplifications limited the applicability of these models to general reactor configurations. For example, the two-dimensional depth averaged model does not take into account of the free surface in an open channel reactor. Therefore, its effect on the hydraulics and disinfection process is not accounted for. The width averaged two-dimensional model would provide inaccurate results as it neglects effects coming from the side walls. As the disinfection characteristics of the reactor is dependent on turbulent mixing within the reactor, two-dimensional model neglects the three-dimensional effect of turbulence and any secondary flow features that are governed by turbulence. Moreover, in a two-dimensional approximation, the cylindrical shape of the lamp cannot be properly accounted for. For this reason the USEPA guideline also suggests that for investigating the reactor performance a three-dimensional model should be considered.

However, three-dimensional simulation is computationally expensive if all the geometrical details of the reactor are included in the simulation. A balance between the accuracy and the computational cost needs to be considered. For this reason the geometry of the reactor needs to be simplified, for example the cleaning system and the inlet and outlet reservoir can be removed to reduce the computational cost, and a simplified lamp support system or without the support can be used. Once validated, the simplified geometry would be used for analyzing different configurations of the lamp banks and other parametric studies.

1.4 Objectives of this Work

The objective of this study is to develop a three-dimensional CFD model for studying the disinfection characteristics of an open channel UV wastewater disinfection reactor with

horizontally arranged UV lamps. Then, a parametric study of the UV reactor is performed using the proposed CFD model to understand the effects of operating parameters such as water flow rate and UV transmittance (UVT). The effect of UV sensitivity of the microbes to be treated on the disinfection performance of the reactor is also investigated.

In wastewater treatment plants, the lamp banks can be placed in series within the open channel to increase the inactivation. The geometric parameters, such as channel constriction/expansion between the lamp banks, can affect the additive nature of the dose delivered. The proposed CFD model is also used to investigate the effect of the geometric parameters on the hydrodynamic and disinfection behavior of the reactors with particular attention to the additive behavior of the delivered dose.

Due to the size of the open channel UV disinfection systems, evaluating their performance experimentally at the design stage is not economically feasible, especially for design optimizations. A small scale reactor which can predict the behavior of the large scale system, would be highly beneficial, to experimentally verify the proposed design. However, due to the interaction of hydraulics, optics and microbial inactivation kinetics, scaling down the UV reactor may be complicated. A scaling methodology for both hydraulics and the disinfection characteristics needs to be formulated. One way to verify the developed methodology is to implement that numerically through the developed CFD model. The disinfection characteristics of the full size and the scaled down reactors predicted by the CFD model can be compared to verify the validity of the developed scaling methodology. Therefore, another objective of this work is to investigate the scalability of the UV disinfection reactor through CFD simulations.

In summary the objectives of this work are:

1. To establish a three-dimensional CFD model that is capable of predicting the disinfection performance of the UV reactor.
2. To perform a parametric analysis to understand the effect of different operation parameters on the disinfection performance.
3. To understand the additive nature of disinfection performance for reactors with two lamp banks using different geometric configurations between the lamp banks.

4. To investigate the possibility of having a small scale model to predict the performance of a full size system.

1.5 Outline of the Thesis

This thesis is organized in five chapters. A brief description of the topics discussed in the following chapters is provided below:

- ❖ Chapter 2-Literature Review
 - This chapter provides a detail discussion of the previous research works relevant to the current study.
- ❖ Chapter 3-Description of the Numerical Model
 - In this chapter, a comprehensive description is provided for the developed numerical model. The boundary conditions and the numerical solution techniques are discussed. The detail descriptions of the reactor geometry and grid generation are provided. At last the scaling down methodologies for both the hydraulics and the optics are explained in detail.
- ❖ Chapter 4-Results and Discussion
 - The grid sensitivity analysis is performed first and then the model is validated against the available experimental data. Then, the validated model is used to investigate the hydraulic and disinfection behavior of the reactor under different flow conditions and geometric parameters. The effects of optical characteristics of the water and the UV sensitivity of different microbes on the disinfection performance are also discussed. At last the validity of the developed scaling down methodology is discussed by comparing the hydrodynamic and the disinfection behavior of the full size and 10 times scaled down reactor.
- ❖ Chapter 5-Conclusions
 - The research findings are summarized.

Chapter 2

2 Literature Review

In this chapter a comprehensive literature review is presented on the numerical simulation of UV disinfection reactors. A majority of the previous studies were performed on the closed channel UV reactors and a few were reported on the reactors having open channel configuration. To understand the effect of different aspects of the computational model, studies on both of these reactor types are discussed.

A gap in the literature is identified in terms of the free surface tracking schemes and the comparative advantages/disadvantages of different turbulence models in the open channel UV disinfection reactors. This gap has arisen because all the previous works in this field were based on two-dimensional depth averaged models and the effects of the free surface were neglected.

2.1 Application of Different Computational Models in UV Reactor Simulations

The numerical simulation of a UV disinfection reactor requires detail calculation of the hydraulics, optics and the disinfection occurring inside it. To resolve the turbulent fluid motion, the Reynolds averaged Navier-Stokes equation is widely used along with a turbulence model. The advantages or disadvantages of different turbulence models usually vary based on the application being modeled. Therefore, an assessment of their applicability is necessary before adopting one. For the disinfection application, another important aspect is the accurate calculation of the UV intensity field since it affects the accuracy of the final inactivation predicted. The merits/demerits of the available computational models for calculating the UV intensity field need to be investigated. The last part in the computational model would resolve the transport of the microorganism and its disinfection. Two general approaches are usually taken to model that: 1) the disinfection field is considered as a continuum and solved in an Eulerian framework and 2) the microorganism particles and their inactivation are tracked using a Lagrangian frame of reference. The applicability of both of these approaches also needs to be

investigated. In this section different studies are reported in a chronological order in an attempt to elucidate the advantages and shortcoming of these above mentioned aspects of the computational model.

One of the earliest attempts to simulate the UV disinfection reactor was accomplished by Downey et al. (1998). They used a computational fluid dynamics model composed of Reynolds averaged Navier-stokes equation and the standard $k - \epsilon$ turbulence model to simulate the liquid flow in a closed channel reactor. The microorganism particle trajectory was calculated in a Lagrangian frame of reference. The residence time of those particles in the reactor outlet was compared with that achieved from the salt tracer test experiment. They reported that at lower flow rates the predicted residence time distribution was within 95% confidence interval with reference to the experimental values. However at higher flow rates the predicted residence time was underestimated. The study was only limited to the calculation of the flow field inside the reactor. The model did not include the calculation of the UV intensity field and consequently the dosage delivered by the reactor was not calculated.

The first study reported in the literature on the simulation of an open channel UV reactor was the work by Lyn et al. (1999). They used a steady two-dimensional depth averaged model to predict the turbulent flow in a vertical type open channel UV reactor. Since the depth averaged two-dimensional model was used, the effect of the free surface was not accounted for. The flow model was based on Reynolds averaged Navier-Stokes equation and the $k - \epsilon$ turbulence model. The predicted velocity was compared with Laser Doppler anemometry (LDA) data. They reported good agreement in the velocity field at the upstream of the channel. However, at the wake region of the lamps, the predicted flow field showed some deviations compared to the experimental measurements. The UV intensity field was calculated using the point source summation (PSS) technique and the disinfection was modeled in an Eulerian framework. They reported that at higher flow rates the disinfection prediction was satisfactory, however, deteriorated at low flow rates.

Chiu et al. (1999a) integrated the dose response information found from a fully mixed batch reactor to a dose distribution curve in actual reactors. The dose distribution was

found from a model that combined the velocity field obtained from experimental measurements using Laser Doppler velocimetry, the particle trajectory information from a Discrete Random Walk (DRW) model based on the measured velocity field and the UV intensity field from a PSS model. The exit dose for the microorganism particles was calculated by performing a time integration of the radiation intensity along their trajectories within the reactor. They found that tracking around 10,000 particles can provide an accurate representation of the dose distribution when using the DRW model. The exit dose distribution calculated from this model matched quite well with the experimental disinfection data from a pilot scale vertical type open channel UV reactor. They hypothesized that this disinfection tracking on a Lagrangian framework can accurately represent the physics of the overall disinfection process. However, the effort and time necessary to obtain the turbulent velocity field experimentally was a limitation to this approach. Therefore, they suggested the use of computational fluid dynamics to resolve the flow field variables.

In a continuation work, Chiu et al. (1999b) considered some design modifications to improve the disinfection performance of the vertical type open channel UV reactor. In the previous study, they noticed that there exist some critical paths for the microorganism particles, which leads to the poor performance of the disinfection process. These paths are from the regions away from the lamps where the UV intensity is low and the fluid velocity is high, therefore, dosage they received is low. To mitigate this problem, they modified the reactor geometry by placing waviness and baffles on the channel walls. The disinfection from these modified systems had improvements over the original one. Their developed model showed good agreement with the experimental data at the medium to high velocities. However, at a lower velocity, they noticed some deviation in the numerical predictions of the disinfection. They attributed this deviation to the inherent inaccuracy in the dose-response kinetic model used to represent the microorganism.

Wright and Hargreaves (2001) performed a comparative analysis for the use of different turbulence models, namely, the standard $k - \epsilon$, RNG $k - \epsilon$ and Reynolds stress models, for the simulation of an annular UV reactor. They reported that, in terms of the predicted dosage distribution and the velocities in the reactor, there was almost no difference

between the results obtained from these turbulence models. The Reynolds stress model predicted slightly different turbulent kinetic energy. However, this difference had little effect on the velocity and consequently disinfection prediction. They concluded that the use of standard $k - \epsilon$ model was sufficiently accurate for disinfection prediction.

Liu et al. (2004) performed a detailed evaluation of several computational models to calculate the UV intensity around a lamp placed in both air and water. They studied the line source integration (LSI), modified LSI, multiple points source summation (MPSS), multiple segment source summation (MSSS), UVCalc3D, view factor and discrete ordinate (DO) model. The UVCalc3D is a commercial code which uses the MPSS approach, and includes the refraction, absorption and scattering effects of the lamp quartz sleeve through a correction factor. They included the refraction effect of quartz sleeve thickness via refraction angles in the MSSS model. The effect of the quartz sleeve was incorporated to the LSI model by the use of attenuation factor. The modified version of the LSI accounted for the radial emission of light from the cylindrical lamp surface. They neglected the effect of refraction and scattering while implementing the DO model. The calculated UV intensity was compared with the experimental measurements using spherical actinometers. For the experiments, they chose ultraviolet transmittance (UVTs) values of 77 and 88 [%/cm] for the water sample. They found that MSSS, LSI and the UVCalc3D approaches provided good match with the experimental data. They found that using the DO model, the UV intensity was overpredicted near the lamp and underpredicted in regions far from the lamps. They suggested that this discrepancy is due to the negligence of the refraction effect at the lamp quartz sleeve. The results showed that all the models that neglected the effects of refraction deviated significantly from the experimental data. They found that both the LSI and the UVcalc3D are computationally inexpensive compared to the MSSS or MPSS approach, as those do not solve for the effects of quartz sleeve rather incorporates its effect through a correction factor. However, their accuracy is similar to the MSSS approach. Therefore, calculating the effect of quartz sleeve in the model is not that important since its effect could be easily and accurately accounted for by using a correction factor. They concluded that in terms of the associated computational cost, the MSSS model is suitable only for reactors having low number of lamps (i.e. six or lower).

Lyn (2004) used the standard $k - \epsilon$ turbulence model to simulate the open channel UV disinfection reactor having vertical arrangement of the lamps. They used a two-dimensional depth averaged computational model. This study was mainly focused on evaluating the effect of unsteadiness due to the vortex shedding from the vertical lamp array on the prediction of the dosage distribution in the reactor. They compared the time averaged unsteady solution with the solution found from a steady state analysis. They found that the difference in the prediction between the time-averaged and the steady state solution was higher in the entrance region of the vertical lamp array and lower in the downstream. They compared these results with the experimental data and found that the time-averaged unsteady model prediction was in better agreement. However, the turbulent kinetic energy was underpredicted in both of these models. Lyn and Blatchley (2005) used the same two-dimensional CFD model for an open-channel vertical type UV system and compared the Lagrangian approach to the Eulerian approach to track the disinfection in the reactor and found similar results in the inactivation of the microorganisms.

Ducoste et al. (2005) used the RNG $k - \epsilon$ model to simulate a closed channel UV reactor. They used both the modified LSI model and the MPSS model based commercial code UVcalc3D to calculate the UV intensity field. This study was also mainly focused on evaluating the Eulerian and Lagrangian methods for the disinfection tracking. In the Eulerian method, they calculated the fluence distribution using a flow-weighted and a mass-weighted fraction technique. They mentioned that the fluence distribution calculated by the Lagrangian technique was not sensitive to the size of the particles used to represent the microorganisms, the wall restitution coefficient for particle reflection or the time step resolution used to capture the particle trajectory. They found that the disinfection predicted by both the Eulerian and the Lagrangian methods provided very good match at the reactor outlet and showed reasonable agreement with the experimental bioassay tests. They concluded that both of these methods can be used alternatively for tracking the disinfection in an UV reactor.

Sozzi and Taghipour (2006) used the realizable $k - \epsilon$ model to simulate an annular closed channel single-lamp UV disinfection reactor for different geometric configurations

of the inlet and outlet ports. This work was also focused on comparing different computational techniques (Lagrangian vs. Eulerian) for calculating the dosage distribution inside the reactor. They used the LSI and the MPSS model to capture the UV intensity field inside the reactor. Predicted dose distributions from both the Lagrangian and Eulerian model showed very good agreement with each other at higher flow rates, however, exhibited slight discrepancy at lower flow rates. The computed dose distribution showed very good agreement with the bio-dosimetry data obtained from an industrial prototype UV reactor.

Elyasi and Taghipour (2006) simulated a close channel annular UV reactor. They used the realizable $k - \epsilon$ model for resolving the turbulence. The disinfection was tracked in an Eulerian framework. Based on the model that they validated, they suggested that the Eulerian approach of disinfection tracking has some advantages over the Lagrangian approach. As an example, they showed that the local volumetric rate of inactivation can be better captured by the Eulerian approach, thus providing insight for better reactor design.

Pan and Orava (2007) evaluated disinfection performance of a closed channel UV reactor for different geometric and flow configurations. They used the standard $k - \epsilon$ turbulence model at the core flow region and an algebraic model at the boundary layer region. They used the MPSS model to resolve the UV intensity and an Eulerian approach to calculate the disinfection performance.

They mentioned that the accurate prediction of the UV intensity is dependent on the efficiency of the lamp, quartz transmittance and the extent of reflection at the walls. However, the uncertainties associated with these variables have less influence on the accurate calculation of the disinfection efficiency of the reactor. They concluded that the reactor's disinfection performance/accuracy is mainly dictated by the flow conditions and the orientation of the lamps inside the reactor, which can produce wide differences in the disinfection performance.

Liu et al. (2007) used six turbulence models, the standard $k - \epsilon$ model, RNG $k - \epsilon$ model, $k - \omega$ model, revised $k - \omega$ model, Reynolds stress transport model (RSTM) and

two-fluid model (TFM) to resolve the flow field in a closed conduit UV reactor. They validated the predicted velocity values and the turbulent kinetic energy with experimental data obtained using the digital particle image velocimetry (DPIV). They found that both the standard and RNG $k - \epsilon$ models exhibited fairly good match with the experiments in predicting the velocity field at different locations inside the reactor. The RSTM exhibited better match in the velocity field. In predicting the turbulent kinetic energy, the $k - \omega$ model showed greater deviation from the experimental measurements. They pointed out that the discrepancies between the predicted velocity and turbulence field were mainly in the wake region of the lamps. They used the MSSS model to calculate the UV intensity field and a Lagrangian particle tracking approach to calculate the dosage on the microorganism particles. Their results showed that the dosage distribution and consequently the inactivation rate were sensitive to the turbulence model selected. For example, turbulence models which predicted larger wake region behind the UV lamps exhibited a broader dosage distribution. The sensitivity of the microorganism was also a contributing factor to these deviations. The microorganisms having a higher UV sensitivity showed greater sensitivity to the turbulence model selection.

Munoz et al. (2007) used a three-dimensional CFD model to predict the performance of a full-scale closed channel UV reactor for disinfection of drinking water. They used both the $k - \epsilon$ model and the RSM to resolve the turbulence field. The predicted velocity and turbulence variables from these two models were almost the same. The difference between the predicted reduction equivalent doses among these models was less than 4%, thereby suggesting that the effect of turbulence model was not prominent in calculating the disinfection. They used the Lagrangian particle tracking with the Discrete Random Walk (DRW) model to resolve the microorganism trajectory. To resolve the UV intensity field, the commercial code UVCalc3D, which is based on MSSS, was used. They developed an approach to investigate the sensitivity of number of Lagrangian particles used in DRW model for calculating the dose distribution. They found that around 30,000 particles can provide insensitive results. The Lagrangian time constant of 0.15 for the $k - \epsilon$ model and 0.3 for the RSM provide reasonably accurate result when DRW is used. They reported that the unstructured tetrahedral mesh predicted different values than the

unstructured hexahedral mesh with same level of resolution. Based on that, it was suggested that the unstructured tetrahedral mesh should be used in caution. The effect of unsteadiness in the flow field on the calculated disinfection was also evaluated. They found that the computed inactivation and the reduction equivalent dose in the unsteady model varied less than 2% compared to the steady model. Based on this finding, they suggested that the steady state model is adequate for the disinfection prediction.

Wols et al. (2010) simulated a UV bench-scale reactor using a CFD model and validated with experimental techniques. They used salt particles to measure the residence time distribution, dye injection to visualize the mixing patterns and LDA measurement to calculate the local velocity profile. The CFD model comprised of the standard $k - \epsilon$ turbulence model, MPSS for fluence field calculation and Lagrangian particle tracking for disinfection calculation. They found that the velocity field has good comparison with the experimental data, however, failed to capture the recirculation region, especially at the wake of the lamps. They also reported that the CFD model predicted higher mixing rate compared to experimental measurements resulting in a narrower residence time distribution.

Younis and Yang (2010) studied the effect of vortex shedding on vertically arranged lamps in an open channel UV reactor. They adopted a depth averaged two-dimensional computational model. They showed that the flow field is inherently unsteady due to the regular shedding of vortices from the vertically arranged lamps. They also showed that the accuracy of the predicted disinfection is strongly dictated by the ability of the computational model to capture the unsteadiness and turbulent mixing arising from the vortex shedding. In a later work, Younis and Yang (2011) reassessed the importance of the above mentioned vortex shedding on the disinfection performance of the UV reactor, especially at the high Reynolds number regime. They used the unsteady form of the governing equations, which included a modified version of the $k - \epsilon$ model that incorporated the effect of vortex shedding on the turbulence energy spectrum. The particle trajectories calculated using the Lagrangian approach along with the modified turbulence model showed wide variation in time due to the vortex shedding, which suggests the effect of vortex shedding should be incorporated in the CFD model.

2.2 Application of Free Surface Tracking Schemes and Turbulence Models in Open Channel Flow Simulation

It is evident from the above section that all the simulations on the open channel reactors performed so far adopted the depth averaged two-dimensional representation of the reactor. Therefore, the water-air interface tracking technique has remained un-discussed. Since a three-dimensional model is used in this study to incorporate the effect of the free surface, the vast area of the open channel flow simulation is briefly discussed in this section to find out the available and mostly used models to track the water-air interface.

Tracking a free surface in a numerical simulation includes an extra difficulty to the computational model. Usually there are two approaches to tackle this problem, the first one tracks the interface in a Lagrangian fashion and the second one uses a fixed Eulerian mesh and solves a transport equation for the volumes of the individual fluids forming the interface.

The first method (i.e. Lagrangian interface tracking) can accurately capture the deformable interface by moving the mesh nodes at those points at a velocity equal to the normal local fluid velocity. However, cases which include large movement of the interface, the mesh deteriorates seriously at those points. To prevent that, the Arbitrary Lagrangian Eulerian (ALE) method was introduced. Literatures provided few instances of using this method in the application of open channel flow (Srinivas, 1992; Ming-Hsi et al., 2001). This approach was not adopted in open channel flow simulations, mainly because of the associated higher computational cost. However, this method has reserved its applications for the fluid-structure interaction problems.

In the second approach, a fixed Eulerian mesh is the basis for the computation and the interface is tracked by solving a transport equation of the fluid volumes. Within this category, the Volume of Fluid (VOF) method has received widespread use. This is mainly due to its low memory and processing power requirements. A brief review on the literature is presented below to evaluate its applicability for the open channel flow simulation.

Abbaspour et al. (2009) used the VOF method to study the hydraulic jump (increase in free surface height) after a sluice gate. They used a two-dimensional approximation with the standard and RNG $k - \epsilon$ turbulence models. They have shown that the VOF method can accurately capture the rise in water-air interface and the predicted free surface values were within a range of 1-8.6% of experimental measurements.

Patil et al. (2009) simulated the open channel flow over bridge decks on different flooding conditions. They used the transient implementation of the VOF to capture the free surface and the RNG $k - \epsilon$ for the turbulence. They have mentioned that the transient VOF is sensitive to the computational input parameters and showed slight deviation from the limited experimental data.

Akoz et al. (2009) compared the experimental values of velocity and free surface profiles along a sluice gate with the computational ones. They showed that both the free surface and the velocity profile were accurately predicted by the computational model, which used the VOF method for interface tracking and the $k - \epsilon$ model for turbulence.

Cassan and Belaud (2012) studied the flow characteristics in the upstream and downstream of a sluice gate. The two-dimensional computational model was composed of VOF method for free surface tracking, RNG $k - \epsilon$ model and RSM for turbulence. They found very good agreement in the predicted velocity profile and head loss in the sluice gate, when compared to the experimental values.

Considering these successful applications of the VOF model in open channel flow simulations and the associated low computational cost, this approach is adopted in this study to capture the water-air interface in the open channel UV reactor.

Open-channel flows usually have complicated flow structures, even for a channel with a simple geometry. For example, the channel with a simple rectangular cross section might have secondary flow features and complicated turbulence field at the free surface. The turbulence field might have severe anisotropy resulting from the interaction of the free surface and the channel side walls. To evaluate the applicability of different turbulence models in open channel flow simulations, a brief literature review is provided below.

Within the Reynolds averaged Navier-Stokes approaches, the two equation $k - \epsilon$ turbulence model and its different variations have been applied extensively for open channel flow simulations (Sinha et al., 1998; Wu et al., 2000; Smolentsev et al., 2002; Ma et al., 2002; Rameshwaran and Naden, 2003; Nezu and Sanjou, 2006; Jha and Bombardelli, 2009; Patil et al., 2009) These two equation models assume the isotropy in turbulence through the Boussinesq approximation. However, this approximation is not always valid in open channel flows. For example, in straight open channels having rectangular cross section, there might exist a secondary flow feature, which is produced only due to the anisotropy in turbulence (Nezu et al., 1993). Since the $k - \epsilon$ turbulence model assumes isotropic turbulence, it cannot capture these behaviours. To account for the anisotropy in the turbulence field, some researchers have used the algebraic stress model (ASM), which is economical in terms of the computational cost (Demuren and Rodi, 1984; Sugiyama et al., 2006; Cea et al., 2007). However, since the ASM does not solve the exact equations for Reynolds stresses, rather uses empirical relationships, the accuracy of the model prediction is highly problem dependent. To overcome this issue, the Reynolds stress turbulence model has been successfully used by different researchers (Kang and Choi, 2006; Jing et al., 2009).

2.3 Conclusion

After investigating the aforementioned studies on both UV reactors and general open channel flow simulations, both $k - \epsilon$ and the RSM turbulence models are adopted in this study to capture the detail turbulent flow characteristics inside the reactor.

The unsteadiness due to the vortex shedding from the lamps, as pointed out by Younis and Yang (2011), was for a reactor having vertical arrangement of the lamps. In this study the lamps are placed parallel to the stream-wise direction. Thus, this effect can be ignored. Based on the findings of Munoz et al. (2007), the steady state approximation led to very similar results in comparison to the time averaged unsteady simulation. Therefore, a steady state approximation is adopted in this study to reduce the computational effort.

To resolve the UV intensity, the DO method without the refraction component is adopted in this work. Liu et al. (2004) mentioned that the DO model overpredicted the UV

intensity near the lamps. They suggested that this discrepancy is due to the negligence of the refraction effect at the lamp quartz sleeve. Bolton (2000) found that for water samples with higher UVT (equal or more than 70%) significant error (up to 25%) arises in the calculated UV intensity field if the effect of refraction is neglected. Since Liu et al. used water samples with ultraviolet transmittance (UVTs) values of 77 and 88 [%/cm], their finding goes well with Bolton's finding. Bolton also suggested that in most wastewater applications where the UV disinfection is used, the UV transmittance values are usually much less than 70%. Thus, discarding the refraction causes only a minor error. Since the UVT of the wastewater in the current study is below 70%, the effect of refraction can be neglected.

Another important point is that the MPSS and MSSS with refraction, reflection and absorption are computationally expensive and could be difficult to deal with while solving for a reactor having multiple lamps. Bolton (2000) showed that the number of point sources should be greater than 1,000 to produce an accurate representation of the UV intensity around the lamp. Therefore, from the computational cost point of view, the DO model is suitable for this study.

All of comparative studies on the Eulerian and Lagrangian approach for the disinfection tracking suggested that both of these approaches produce the results with similar levels of accuracy. Therefore, the Lagrangian approach is chosen as it is more intuitively promising and enables the visualization of the low/high dosed particle trajectory inside the reactor, thus providing insight of the whole disinfection process at a glance.

The VOF model is adopted for this study based on the successful implementation of this model to capture the water-air interface for general open channel flow simulations and considering the associated low computational cost.

From the above literature review, it can be noticed that several works have been presented using the two-dimensional depth averaged model for the open channel UV reactors having vertically arranged lamps (Lyn et al., 1999; Lyn, 2004; Lyn and Blatchley, 2005; Younis and Yang, 2010; Younis and Yang, 2011) whereas, no studies have been reported on the reactors having horizontally arranged lamps. Therefore, the

current study focuses only on the horizontal type of the open channel UV reactor. Since literature provides no evidence on the study of the reactors having two lamp banks placed in series, this work intends to fill that gap. This study will investigate another aspect of the open channel UV reactors, i.e. the scalability, since no information can be found on the literature regarding that.

Chapter 3

3 Description of the Numerical Model

In this chapter, the geometric configuration of the reactor will be presented first. Then, a detailed description will be provided for the numerical model proposed in this study. The boundary conditions and the numerical solution techniques will be discussed. A brief description of the grid generation procedure will be provided along with the snapshot of the grids used in this study. At last the scaling down methodology for both the hydraulics and the optics will be explained in detail.

3.1 The Reactor Geometry

The reactor used in this study is an open channel reactor with one bank of lamps placed inside the reactor horizontally, which is parallel to the main flow. The bank is composed of 24 lamps, 4 in the lateral direction and 6 in the vertical direction. The vertical assembly of 6 lamps are called modules. The lamps are low pressure UV lamps with 92W power rating, which emit nearly monochromatic light at 253.7 nm wavelength. This wavelength is close to the germicidal inactivation peak for *E. coli* and *Cryptosporidium* (Linden et al., 2001). The electrical efficiency of the lamps is assumed to be 100%. It is also assumed that the full lamp power is used for the light emission in the narrow wavelength range of 253 to 255 nm. The effect of fouling on the lamp sleeve surface is ignored.

Figure 3.1 shows the schematic diagram of the computational domain used in this study without the lamp support system, and the inlet and outlet reservoirs to reduce the computational cost. The inlet and outlet reservoirs are not included to reduce the computational domain length and they are taken care of by implementing appropriate boundary conditions at the inlet and outlet in the CFD model as described later. The dimension of the computational domain is also shown in Figure 3.1. The diameter of the lamp sleeve is 0.028 m and the spacing between the lamps is 0.0736 m at both vertical and horizontal directions. The inlet and outlet boundaries are placed at an approximate distance of two lamp lengths from the lamp bank. In practical applications, the free

surface is controlled using a weir placed at the downstream of the reactor. In this study, the free surface at the outlet is kept at a height of 0.6096 m.

Another geometry used in the simulation includes a simplified lamp support system to investigate the effect of the lamp support system on the numerical results. The close up of the simplified lamp support system is shown in Figure 3.2.

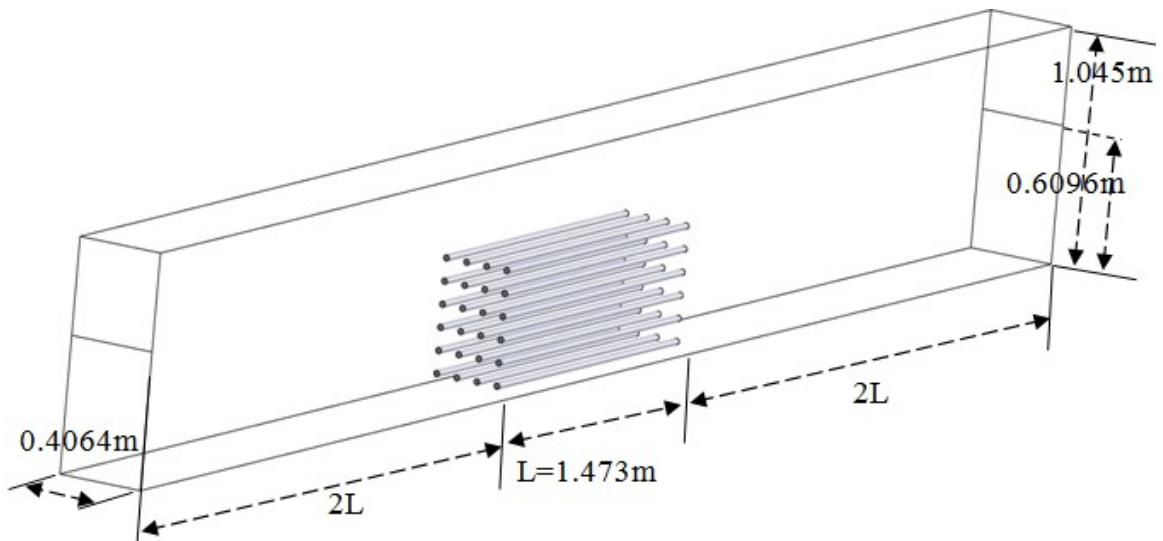


Figure 3.1: Schematic of the computational domain without lamp support system

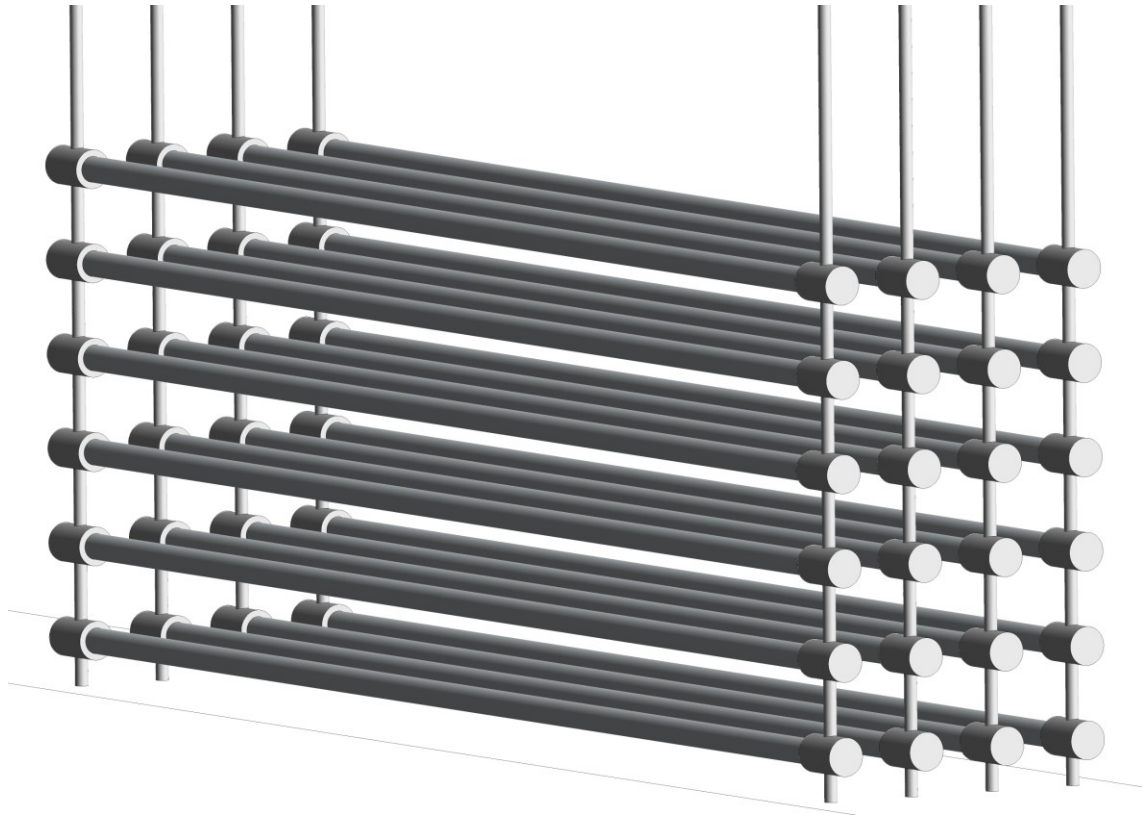


Figure 3.2 Simplified lamp support system

3.2 Computational Model

The computational model is divided into four parts. The first part deals with resolving the flow characteristics in a typical turbulent open channel flow with water-air interface tracking. The second part deals with resolving the trajectories of the microbial particles flowing with the water. The third part is the calculation of the UV intensity field within the reactor. And the final part implements the inactivation kinetics on each microbial particle to calculate the overall log inactivation achievable in the reactor and the reduction equivalent dose (RED) value.

3.2.1 Turbulent Open Channel Flow with Water-air Interface

The volume of fluid (VOF) method is used in this study to capture the water-air interface in the open channel flow. A single set of momentum equations and the continuity equation for the mixture of water and air is solved. Since a steady state solution is sought for the flow variables in the reactor, the unsteady terms are neglected. Since the flow is

turbulent, the Reynolds averaged Navier-Stokes equation is used. The continuity and the momentum equations are given below.

$$\frac{\delta \rho}{\delta t} + \nabla \cdot (\rho \vec{v}) = 0 \quad (3.1)$$

$$\frac{\delta}{\delta t}(\rho \vec{v}) + \nabla \cdot (\rho \vec{v} \vec{v}) = -\nabla p + \nabla \cdot (\bar{\sigma} + \bar{\tau}) + \rho \vec{g} + \vec{F} \quad (3.2)$$

where $\bar{\sigma}$ and $\bar{\tau}$ are the fluid stress tensor and the Reynolds stress tensor. The physical properties in Eqs. (3.1) and (3.2) are obtained from individual fluid properties based on the mixture rule. For example, the density of the mixture is calculated as following:

$$\rho = \rho_w \alpha_w + \rho_a (1 - \alpha_w) \quad (3.3)$$

where α_w and ρ_w are the volume fraction and the density of water, respectively. ρ and ρ_a are the density of the mixture and the air, respectively.

The interface is tracked by solving a transport equation for the volume fraction of the heavier fluid, the water in this case. This is basically a continuity equation for the water phase. The heavier fluid is usually chosen, because satisfying its mass conservation is more important than the lighter fluid. The transport equation is expressed as:

$$\nabla \cdot (\alpha_w \rho_w \vec{v}) = 0 \quad (3.4)$$

Eq. (3.4) is solved with the constraint that the summation of the volume fraction of water and air should be unity. The air volume fraction is calculated accordingly.

The Reynolds stress tensor $\bar{\tau}$ in Eq. (3.2) needs to be modeled to close the governing equations. For this purpose the eddy-viscosity concept or the Boussinesq approximation is used. In Boussinesq approximation, the Reynolds stress is expressed in terms of the mean velocity gradients and two new quantities namely, turbulent viscosity μ_t and turbulent kinetic energy k . The expression for the Reynolds stress $\overline{v'_i v'_j}$ in indicial notation is shown as:

$$-\rho \overline{v'_i v'_j} = \mu_t \left(\frac{\delta v_i}{\delta x_j} + \frac{\delta v_j}{\delta x_i} \right) - \frac{2}{3} \left(\rho k + \mu_t \frac{\delta v_k}{\delta x_k} \right) \delta_{ij} \quad (3.5)$$

where v' represent the fluctuating component of the velocity and v represents the mean velocity. Subscripts i and j represent the coordinate directions. The turbulent kinetic energy k is the energy per unit mass of the fluid associated with the turbulent fluctuating motion and is defined as:

$$k = \frac{1}{2} (\overline{v'^2_i} + \overline{v'^2_j} + \overline{v'^2_k}) \quad (3.6)$$

To solve for k and μ_t two additional transport equations are necessary. In this work, the realizable $k - \epsilon$ turbulence model is adopted. In this model, the transport equations are solved for the turbulent kinetic energy k and its dissipation rate ϵ . The equations are as follows:

$$\frac{\delta}{\delta t} (\rho k) + \nabla \cdot (\rho \vec{v} k) = \nabla \cdot \left(\left(\mu_m + \frac{\mu_t}{\sigma_k} \right) \nabla k \right) + G_k - \rho \epsilon \quad (3.7)$$

$$\frac{\delta}{\delta t} (\rho \epsilon) + \nabla \cdot (\rho \vec{v} \epsilon) = \nabla \cdot \left(\left(\mu_m + \frac{\mu_t}{\sigma_\epsilon} \right) \nabla \epsilon \right) + \rho C_1 S \epsilon - \frac{\rho C_2 \epsilon^2}{k + \sqrt{\mu \epsilon / \rho}} \quad (3.8)$$

where G_k is the production of turbulent kinetic energy due to the mean velocity gradients and C_1 is a function of k , ϵ and mean strain rate. C_2 is a model constant and S is the scalar measure of the deformation tensor. σ_k and σ_ϵ are the turbulent Prandtl number for k and ϵ and assigned constant values, respectively.

The realizable $k - \epsilon$ model differs from the standard $k - \epsilon$ model in terms of the expression for turbulent viscosity. In the standard $k - \epsilon$ model, μ_t is calculated using the following formula:

$$\mu_t = \rho C_\mu \frac{k^2}{\epsilon} \quad (3.9)$$

where C_μ is a constant. However, in the realizable $k - \epsilon$ model, C_μ includes the effect of mean rotation on the turbulent viscosity μ_t and therefore is a function of mean strain and rotation rates, the angular velocity of the system rotation and the turbulence field k and ϵ (ANSYS FLUENT Theory Guide, 2010).

Turbulence is highly affected by the presence of the walls. Near the walls, the viscous damping reduces the tangential fluctuation and the kinematic blocking reduces the normal fluctuation of the velocity. Due to the sharp velocity gradient in the boundary layer near the wall, turbulence is rapidly generated. Therefore, wall functions, which are semi-empirical correlations, are used to bridge the gap between the viscosity dominated sublayer and the core turbulent region. The main benefit of using a wall function is that a relatively coarse mesh can be used as long as the first cell falls in the logarithmic region of the turbulent boundary layer, i.e. the non-dimensional distance from the wall y^+ for the first cell is above 30. The upper limit usually varies according to application (Reynolds number), but in general the value of 200 is considered to provide reasonably accurate result. However, this approach gives erroneous result when the first cell falls in the buffer layer, thus it restricts the grid refinement which is necessary to resolve the whole boundary layer with sufficient number of grid points. Moreover, the near wall effect of turbulence is not well accounted for.

Another approach to resolve the turbulence near the wall is enhanced wall treatment. This approach does not have any stringent requirement for the non-dimensional y^+ for the first cell. The blending of the law of the wall for laminar region to the log law region is used in this approach and the turbulent viscosity within the viscous sublayer to the full turbulent region is calculated using a blending function (ANSYS FLUENT Theory Guide, 2010).

The Reynolds stress model is also used to capture the flow features that might exist in the reactor resulting from the anisotropy of the turbulence. This model does not rely on the Boussinesq approximation to relate the Reynolds stresses to the mean flow gradients, rather it solves transport equation for all the components in the Reynolds stress tensor along with the equation for the dissipation rate of turbulent kinetic energy. In three-

dimensional simulations, this model requires 7 additional transport equations to be solved. The transport equations are not listed here and can be found in the ANSYS FLUENT Theory Guide (2010).

3.2.2 Microbial Particle Trajectory

The microbes are modeled as spherical particles having an average of 1 micron diameter. Ducoste et al. (2005) showed that the disinfection predicted by the Lagrangian tracking is not sensitive to the diameter of the particles used. The density of the particles is taken to be same as the density of water, which is based on the fact that most of the microbes have almost 70% or more water content in them. The trajectories of the microbial particles are calculated by integrating the force balance on the particles in a Lagrangian frame of reference. The force balance in the x -direction can be expressed as:

$$\frac{d\vec{v}_{xp}}{dt} = \frac{18\mu_m C_D Re}{\rho_p d_p^2} (\vec{v}_{xw} - \vec{v}_{xp}) + \frac{\vec{g}_x(\rho_p - \rho_w)}{\rho_p} \quad (3.10)$$

where d_p is the particle diameter and Re is the relative Reynolds number based on particle diameter and the relative velocity of water and particles. C_D is the drag force coefficient for spherical particles and is expressed as:

$$C_D = a_1 + \frac{a_2}{Re} + \frac{a_3}{Re^2} \quad (3.11)$$

where a_1 , a_2 and a_3 are constants given by Morsi and Alexander (1972). The Brownian motion of the particles are neglected since the velocity magnitude of the microorganism dictated by the carrying water is significantly high as the flow is turbulent. The force on the particles resulting from the pressure gradient in the flow field is also neglected as it is only important when the fluid density is higher than the particle density.

The particle trajectories are calculated based on the instantaneous fluid velocity instead of the mean velocity to include the effect of turbulence on the dispersion. The fluctuating component of the velocity is calculated using the discrete random walk model, which randomly assigns the velocity based on the characteristic life time of the eddy and the integral time scale of the Lagrangian particles. The integral time scale T_L which describes

the time spent in turbulent motion along a particle path is calculated from the turbulent kinetic energy and its dissipation at every point.

$$T_L = 0.15 \frac{k}{\epsilon} \quad (3.12)$$

In the DRW model the interaction of a particle with successive fluid phase eddies are included. Each eddy is characterizing by a eddy life time and a Gaussian distribution of the fluctuating velocity.

$$u' = \zeta \sqrt{u'^2} = \zeta \sqrt{\frac{2k}{3}} \quad (3.13)$$

here, ζ is a normally distributed random number. The characteristic life time of the eddies τ_e are calculated from the following

$$\tau_e = -T_L \ln(r) \quad (3.14)$$

here, r is a uniform random number between 0 to 1. The particle is assumed to interact with the fluid phase over the smaller of the eddy lifetime and the eddy crossing time. When this time is reached a new value of the instantaneous velocity is obtained by applying a new value of ζ . By computing the trajectory for a sufficient number of representative particles, the random effects of turbulence on the particle dispersion can be accounted for.

3.2.3 UV Intensity Field

The UV light while propagating from the lamp surface interacts with the medium by four different ways: absorption, reflection, refraction, and scattering. Brief descriptions of these phenomena are given below:

- 1) Absorption refers to the change in the intensity due to the conversion of the light energy to other forms, while it passes through a medium.
- 2) Refraction refers to the change in the direction of the light due to the change of the medium at the interface.

- 3) Reflection refers to the change in the direction of the light after hitting a surface, specular/diffuse.
- 4) Scattering refers to the change in the direction of the light propagation after hitting a suspended particle in the medium.

The effect of absorption and scattering depends on the optical qualities of the water being treated. The UV absorption coefficient (a) and the UV transmittance (UVT) are widely used to characterize them.

The UV Transmittance (UVT) is the percentage of light passing through the medium over a specified distance. The UVT is expressed as following:

$$\%UVT = 100 \frac{I}{I_0} \quad (3.15)$$

where $\%UVT$ is the UV transmittance [$\% \text{ cm}^{-1}$], I is the Intensity of light transmitted through the sample [mW cm^{-2}] and I_0 is the Intensity of light incident on the sample [mW cm^{-2}]. I/I_0 is the reduction in intensity over 1 cm.

The absorption coefficient a can be related to the UV transmittance (UVT) by the use of Beer-Lambert's law, which states that the UV intensity decreases exponentially due to the effect of absorption in a homogeneous medium, with zero turbidity (suspended solid particles).

$$UVT = \frac{I}{I_0} = 10^{-ax} \quad (3.16)$$

Usually the value of absorption coefficient of water changes over the wavelength spectrum of the UV radiation. However, since a monochromatic UV at 254nm is considered in this study, the value of a at this wavelength is considered. The turbidity of the medium is assumed to be zero, since the concentration of solid particles is low in pre-treated effluent prior to UV disinfection.

From Eq. (3.16) it can be said that the ratio of the intensities at two subsequent points (1 and 2) will be the same, as long as the distance between the two points is the same. So,

$$\frac{I_1}{I_2} = 10^{-a(x_1-x_2)} \quad (3.17)$$

Therefore, if the distance $x_1 - x_2 = 1$ [cm], $I_1/I_2 = 10^{-a} = UVT$ and the absorption coefficient can be calculated from the UVT as following:

$$a = -\log(UVT) * 100 \quad (3.18)$$

It can be noticed that the absorption coefficient is the slope of the straight line of UV intensity vs. path length plot in a logarithmic scale and the absorption coefficient is in [m^{-1}], 100 is used to convert [cm^{-1}] to [m^{-1}] and the UVT is in the fractional form.

In this study, the UV intensity field is resolved using the discrete ordinate (DO) model, where the radiative transfer equation (RTE) is solved at every control volume for a finite number of direction vectors (solid angles). The number of RTEs increases with the number of discrete solid angles used. The radiation intensity depends on the spatial coordinates, direction vectors and radiation frequency. However, in this work, the frequency dependence is ignored as the low pressure UV lamps are fairly monochromatic. The RTE for a non-gray radiation is expressed as:

$$\nabla \cdot (I(\vec{r}, \vec{s})\vec{s}) + (a + sc_s)I(\vec{r}, \vec{s}) = 0 \quad (3.19)$$

where I is the radiation intensity, \vec{r} is the position vector, \vec{s} is the direction vector and \vec{s}' is the scattering direction vector, a and sc_s are the absorption and scattering coefficient of the medium, respectively. The first term in Eq. (3.19) represents the spatial gradient of the intensity and the second term represents the absorption and scattering loss in the medium. The contribution from the scattering by suspended particles are neglected in this study. The thermal radiation contribution from the medium is neglected in this study since the temperature of the water is low. The energy equation is not coupled with the DO model as there is no considerable change in the temperature of the water during the disinfection process. This is due to the fact that negligible amount of radiation is emitted from the low pressure lamps in the thermal radiation wavelength range.

3.2.4 Inactivation Kinetics

The dose-response relationship of the microbial species is considered to be of the first order, which can be expressed mathematically as:

$$\frac{dN}{dt} = -c \cdot I \cdot N \quad (3.20)$$

where N is the number of potent microbes at any instant, I is the radiation intensity, t is the time of exposure and c is the sensitivity of the microbes to UV, which is considered to be constant over the entire inactivation. The solution of Eq. (3.20) is:

$$\ln \frac{N_0}{N} = c \int_0^t I dt \quad (3.21)$$

where, N_0 is the number of potent microbes at time zero. The integration of the radiation intensity over time is termed as Dose [mJ/cm^2]. In Eq. (3.21), the natural logarithm is changed to 10 based logarithm by correcting the UV sensitivity c with a multiplication factor. The following equation is obtained:

$$\log_{10} \frac{N_0}{N} = \frac{1}{d10} Dose \quad (3.22)$$

It should be noted here that $\log_{10}(N_0/N)$ is usually defined as the log removal or log inactivation. In Eq. (3.22), the quantity $d10 = (1/c) [mJ/cm^2/log]$ represents the UV sensitivity of the microbial species, which represents the required amount of dose for 1 log removal. The significance of $d10$ values is that greater inactivation occurs at lower $d10$ values for the same applied dosage value on the microbe. This dose-response relationship can be expressed as either the proportion of microorganisms inactivated or the proportion of microorganisms remaining as a function of UV dose applied. Microbial inactivation has a dose-response curve with a positive slope, while microbial survival $\log_{10}(N/N_0)$ has a dose-response curve with a negative slope.

The linear inactivation kinetics utilized in this study can represent the microbes, which have nearly linear dose-response relationship. Some representative microbes (two

different virus and a bacteria) are shown in Figure 3.3 which follow a linear dose-response relationship based on the data obtained from Chevrefils et al. (2006). The slope of the straight line corresponds to the $1/d_{10}$ value mentioned in Eq. (3.22). For the microbes plotted in this figure, the d_{10} values are ranging from 1 to 10 [$mJ/cm^2/log$]. However, a wide range of d_{10} values (1 to 25 [$mJ/cm^2/log$]) are considered in this study to cover more microbes, including spore forming bacteria, which are usually difficult to inactivate.

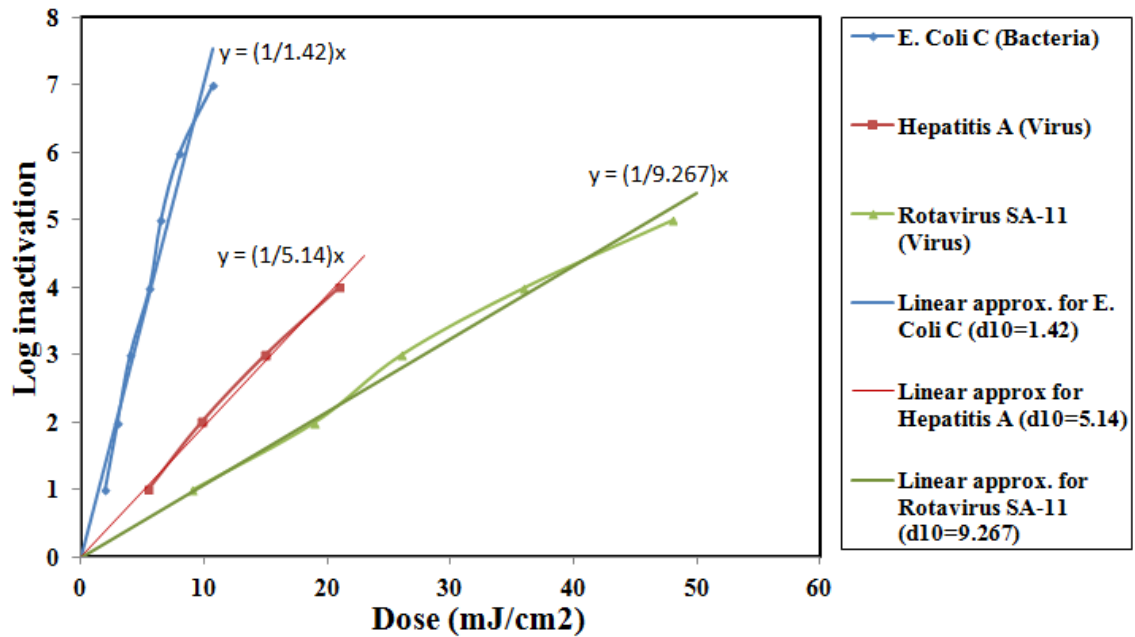


Figure 3.3: Dose-response relationship for some microbes and their approximation to linear kinetics.

In the numerical model, the dose is calculated by the time integral of the radiation intensity over the trajectory of each particle (Chiu et al., 1999a). A custom user defined function (UDF) is developed in the ANSYS FLUENT to obtain the UV dose that a microbial particle is exposed to during its residence time within the reactor. The UDF can be found in Appendix A.

Because of the complex turbulent flow within the reactor and an exponential decay of the UV intensity field around the lamps, each of the microbial particles receives a different UV dose, depending on their trajectories inside the reactor, resulting in different

inactivation rates for different microbial particles. However, an average dose delivered by the reactor needs to be established to quantify its inactivation performance. Therefore, either the survival or inactivation fraction for the microbes has to be averaged over the entire dose range. Based on the average survival/inactivation fraction, the corresponding dose value is calculated from the dose-response relationship of the microbe. This dose value is named as the RED of the reactor. Considering the first order dose-response relationship, the expression for the RED can be mathematically expressed as (Liu, 2004):

$$\text{RED} = -\frac{1}{c} \log_{10} \left(\int_0^{\infty} p(D) \cdot 10^{-cD} dD \right) \quad (3.23)$$

where $p(D)$ is a weighting function, which accounts for the probability of a microbe getting a dose value of D . In the numerical model considered in this study, this $p(D)$ represents the number of microbial particles getting dose in a distinct dose interval. The above integral is evaluated by numerically averaging the survival fractions ($10^{-\frac{1}{d_{10}}D}$) for all the particles and then calculating the log inactivation from that. It should be noted that the probability of occurrence $p(D)$ is taken into account while taking the arithmetic average of survival fractions of all the tracked particles. The higher probability region of dose histogram typically would have more number of tracked particles, thus, the survival fraction or inactivation value in that region gets more weight during summation. To calculate the RED, the corresponding dose value for the average log inactivation is found from the dose-response curve.

The dose values obtained for the particles are exported to MATLAB for further post processing. The postprocessor calculates the log removal and RED obtainable from the reactor. The UV dose delivered by the reactor is best described using a probabilistic distribution of the dosage over the delivered dose range. From the width of probabilistic dose distribution, the inactivation performance of the reactor can be inferred. A narrow distribution would indicate that the reactor is able to deliver similar dosage to all the microbes, whereas a wider distribution would indicate non-uniform distribution of dosage. To visualize this dose distribution, the post processor developed in this study also provides a probabilistic distribution of the dosage over the delivered range.

3.3 Boundary Conditions and Numerical Solution Techniques

In this section, the boundary conditions used for the computational domain shown in Figure 3.1 are summarized. A brief description is also provided on the numerical techniques required to get solutions from the governing equations.

The boundary conditions necessary for the fluid flow equations are summarized in Figure 3.4. To represent the inlet sluice gate, the upper half of the inlet section is specified a no-slip boundary condition and the lower half section is set as a velocity inlet boundary condition corresponding to the mass flow rate of water in the reactor. For turbulence models the wall normal gradient of turbulent kinetic energy is set to zero at walls. The height of the lower half is taken to be the same as the expected free surface height in the reactor, which is 0.6096 m. A uniform velocity profile is assigned since the actual velocity profile at this section is not known. A pressure outlet boundary condition is implemented at the outlet of the reactor. A hydrostatic pressure profile is applied based on the free surface location. The front, back and bottom boundaries are assigned no-slip condition. The top boundary is also considered to be pressure outlet with atmospheric pressure specified there.

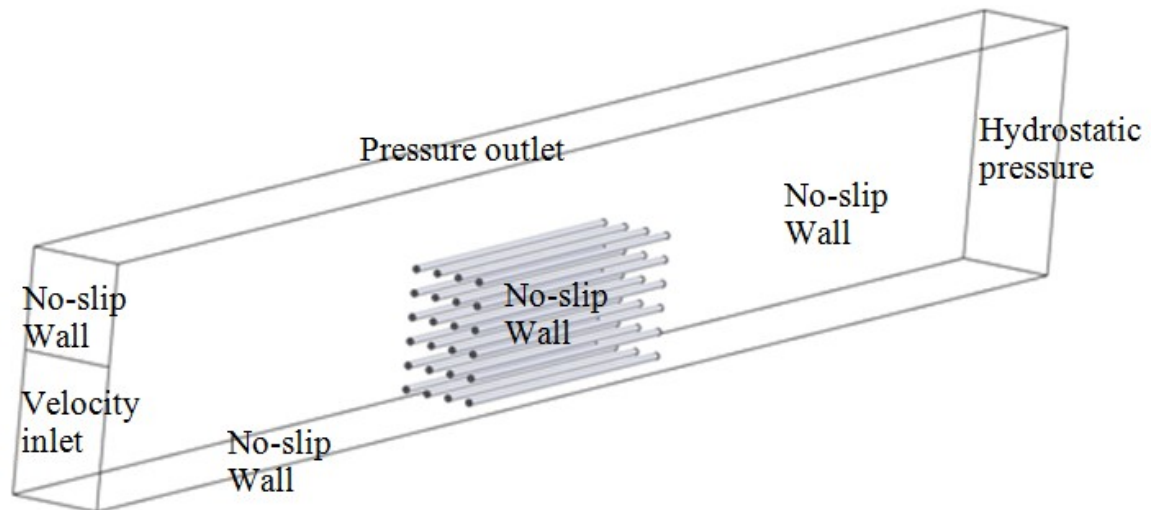


Figure 3.4: Boundary conditions for the momentum and continuity equations

The convergence behaviour of the solution using the multiphase VOF model is sensitive to the initial values used. The volume fraction of water is initialized in the water domain. A hydrostatic pressure based on the depth from the expected free surface height is also initialized.

The discretized form of the transport equation for water volume fraction requires the calculation of the volume fraction flux at a cell face by interpolation from the cell centre values. It was found that the upwind schemes (both second and first order) are highly diffusive, i.e. it results in a diffusive or wider water-air interface. The QUICK scheme was also tried and it provides similar diffusiveness. Therefore, a modified version of high resolution interface tracking scheme (HRIC) is used to solve the transport equation for the volume fraction. The second order upwind discretization is used for all other equations. The least squares cell-based scheme is used to calculate the gradient of the variables.

For the realizable $k - \epsilon$ model, the turbulent intensity at the reactor inlet and the hydraulic diameter are specified. Since this is an internal flow, the importance of the value for the turbulent intensity at the inlet is not critical as most of the turbulence is generated internally within the domain due to the shear in the mean velocity field. Considering the Reynolds number based on the hydraulic diameter of the reactor inlet is in the order of 10^5 , the turbulence intensity at the inlet is specified to be $0.16 * Re^{-1/8} \approx 2 - 3\%$. This expression is based on the turbulence intensity for the fully developed pipe flow.

To make sure that the turbulence is well resolved at the walls, y^+ values of $30 < y^+ < 80$ is used for the models with the higher flow rates. Akoz et al. (2009) found that a good solution could be obtained if the y^+ value is around 30. For lower flow rate cases, $y^+ < 10$ is used, thus, resolving the viscosity affected near wall region ($y^+ < 11$). The y^+ value between 11 and 30 is usually in the buffer layer, i.e. between the viscous sublayer and the log law region ($y^+ > 30$), and should be avoided since there is no good correlation available in this region (ANSYS FLUENT Theory Guide, 2010).

In the Lagrangian particle tracking model, according to Munoz et al. (2007) the number of particles tracked will affect the accuracy of the calculated dose distribution. The multiplication of the number of particles injected and the number of tries are the actual number of particles tracked. To maintain statistical significance of the particle trajectories and the dose values on those particles, around 75,000 particles are tracked at each simulation (25000 particles with 3 tries).

For the particles, a reflect boundary condition is used at the walls with very low normal reflection coefficient to make sure that the particles do not go far away after hitting a wall boundary. Since the free surface position is not known a priori, applying a boundary condition there for the particles is not possible. However, these particles should stay in the water domain. Although neutrally buoyant particles are used, their velocities are governed by the mixture velocity. Therefore, some particles might go to air region following the mixture velocity field. To enforce the particles to stay in the water, a UDF is used which deletes a particle when it reaches a cell with very low water volume fraction.

For the DO model, it is assumed that all the incident radiations at the reactor walls are absorbed and none is reflected. The emissivity of the wall is set to 1 to implement that. At the lamp surface the radiation intensity is applied such that the light is diffusely radiated from that surface and, the electrical lamp power value is divided by the lamp sleeve surface area. The efficiency of the lamp in converting electrical energy to light energy is assumed to be 100%.

To solve the RTE at a given discrete solid angle, the angular space (4π Steradian) needs to be discretized. In this study, both the polar and azimuthal angles are divided into 4 directions. This division is based on the mesh used for solving the fluid flow. While solving the RTE at a control volume, its face may not be aligned with the global angular discretization. Therefore, it might act partially as an incoming and outgoing face for radiation at a particular solid/control angle. This problem, which is termed as the overhanging control angle, is taken care of by dividing overhanging faces into small

chunks, called pixelation (ANSYS FLUENT Theory Guide, 2010). In this study, each overhanging angle is divided into 4x4 pixels.

A pressure based solver is used, where a collocated grid formulation is used, i.e. the velocity and pressure values are stored at cell centres. Therefore, interpolation is necessary to calculate pressure values at the cell faces required by the momentum equation. The Pressure staggering option (PRESTO) is used for that purpose. A segregated solver algorithm is chosen since the flow is incompressible. The SIMPLEC algorithm is chosen for pressure-velocity coupling.

The discretized equations are solved in SHARCNET parallel clusters. The steady state solver is used. The convergence criteria for the residuals are 10^{-4} for continuity equation and 10^{-8} for other equations. The overall mass conservation throughout the domain is monitored along with the velocity value at a point in the reactor outlet.

3.4 Grid Generation

The computational domain is discretized with all hexahedral elements. A multiblock structured mesh is generated using ANSYS ICEM software and then converted to unstructured mesh to read into ANSYS FLUENT. Although hexahedral elements are difficult to generate for complex geometries, this element type is chosen in this study because of its several benefits: 1) it provides good convergence behaviour with less number of elements compared to unstructured tetrahedral, prismatic or pyramidal elements, 2) it shows good grid sensitivity behaviour, 3) element skewness is low for high aspect ratio elements near the walls because of the wall function requirements in the turbulence models, and 4) less discretization error (numerical diffusion) due to the body fitted grid near the curved surfaces and the cells aligned with the mean flow direction (ANSYS FLUENT Theory Guide, 2010).

Figure 3.5 shows the element distribution at a lateral-cut-plane for a coarser mesh in the computational domain. Mesh density is high near the expected free surface region to better capture the fluid flow aspects near the free surface and is high around the lamp region due to the exponential decay of UV intensity field. The hexahedral mesh is also

generated for the geometry with lamp support systems. Figure 3.6 shows the surface mesh on the lamp support and the volume mesh at a lateral-cut-plane.

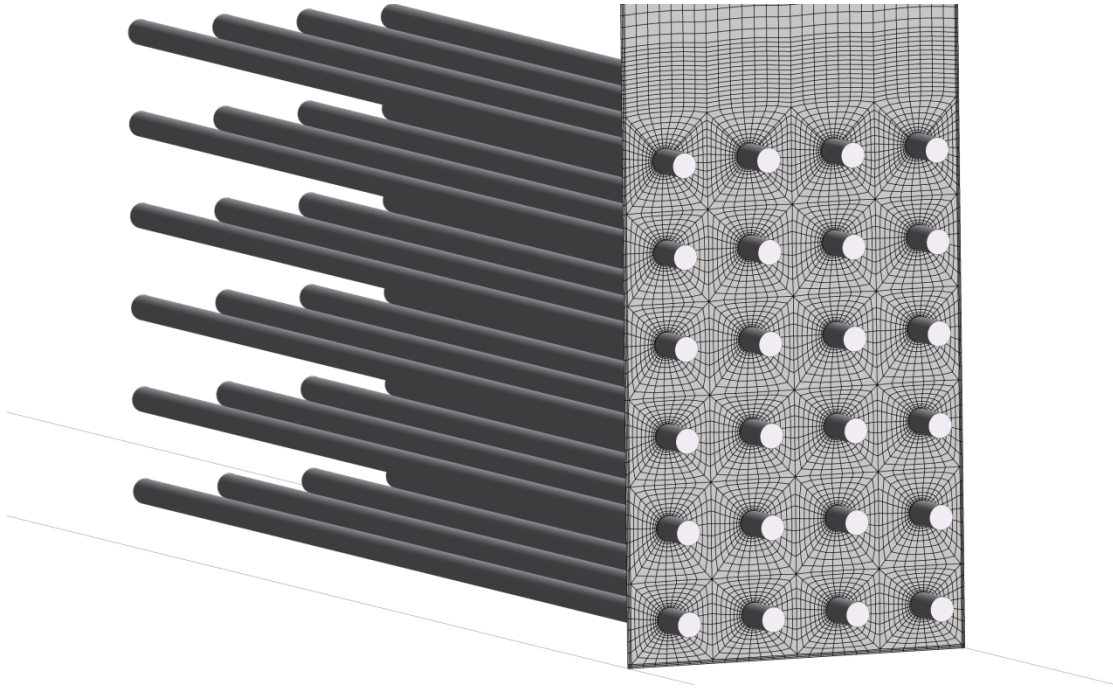


Figure 3.5: Element distribution at a lateral cut-plane for the geometry without the lamp support system

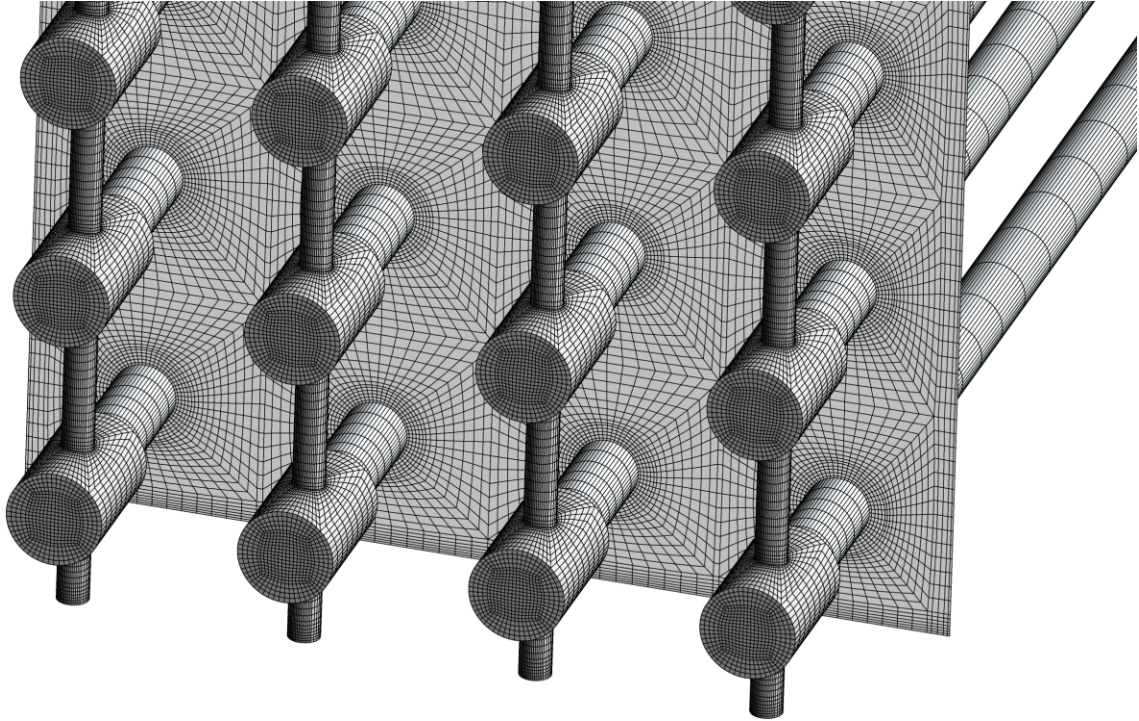


Figure 3.6 The surface mesh on the lamp support and the volume mesh at a lateral-cut-plane.

3.5 Scaling Down Methodology

In this section, the scaling down methodology for the UV disinfection reactor is described. The requirement for the hydraulic similitude is presented from the theoretical background and then the similitude requirement for the radiation field is derived based on the similarity in disinfection performance of the reactor.

3.5.1 Similarity of Hydraulics in Open Channel Flows

Based on similitude analysis, it is well known that the behaviors of two different physical models (full size and small scale) are similar if they are dynamically similar. There are three types of similarities:

1. Geometric similarity - all geometric dimensions should be scaled identically.
2. Kinematic similarity – all streamlines must be similar.
3. Dynamic similarity - ratios of all forces must be the same.

If the geometric similarity and kinematic similarity are maintained, the next objective is to maintain the dynamic similarity by maintaining constant ratio of all forces dictating the physics of the problem. The forces that come into play in open channel flows are:

1. Inertia force
2. Gravitational force
3. Viscous force
4. Surface tension force

The ratios of the magnitudes of the gravitational, viscous and surface tension forces to the magnitude of the inertia force form the three non-dimensional numbers; Froude number, Reynolds number and the Weber number, respectively, used in open channel flows. If these non-dimensional numbers can be maintained constant along with the geometric and kinematic similarities, one can expect that the scaled model would behave the same as that of the full size model. The next subsections describe each of those three non-dimensional numbers and the implication of maintaining them constant for the scaled model and the full size model (termed as prototype hereafter).

3.5.1.1 Froude Number

Froude number characterizes the relative importance of inertia force over gravitational forces. In other words, it represents the ratio of the mean flow velocity with the velocity generated by the gravitational waves (\sqrt{Lg}). Therefore, the Froude number Fr is defined as:

$$Fr = \frac{V}{\sqrt{Lg}} \quad (3.24)$$

where V is the mean flow velocity, L is the length scale, usually taken as the flow depth and g is the gravitational acceleration. Equating the Froude number of the model and the prototype ensures that the gravitational and inertial forces are in the same proportion. If the Froude number is maintained the same between the model (m) and the prototype (p), the following implications would result:

$$\begin{aligned}
Fr_m &= Fr_p \\
\Rightarrow \frac{V_m}{\sqrt{L_m g}} &= \frac{V_p}{\sqrt{L_p g}} \\
\Rightarrow \frac{V_m}{V_p} &= \frac{\sqrt{L_m}}{\sqrt{L_p}} \\
\Rightarrow V_r &\propto \sqrt{L_r} \quad (3.25)
\end{aligned}$$

Implications are:

- ❖ velocity ratio: $V_r \propto \sqrt{L_r}$
- ❖ time ratio: $t_r \propto \sqrt{L_r}$
- ❖ discharge ratio: $Q_r \propto L_r^{5/2}$
- ❖ force ratio: $f_r \propto L_r^3$

Hereafter, ratios are defined as model to prototype (i.e. small scale over full size)

It should be noted here that the velocity ratio resulting from the Froude numbers proportional to the square root of the length scale ratio.

According to Froude number, the open channel flow can be divided into three categories, a) subcritical ($Fr < 1$), b) critical ($Fr = 1$) and c) supercritical ($Fr > 1$) flow. For the maximum velocity $1.1 [ms^{-1}]$, the Froude number in the reactor will be $0.45 (< 1)$, if the flow depth of $0.6096 [m]$ is taken as the length scale. For lower flow rates, the Froude number is even smaller suggesting that the reactor studied in this work operates in the subcritical range at all flow rates.

3.5.1.2 Reynolds Number

Reynolds number Re is defined as the ratio of the viscous force and inertia force:

$$Re = \frac{\rho V L}{\mu} \quad (3.26)$$

where $\mu [kg m^{-1} s^{-1}]$ is the dynamic viscosity and ρ is the density of the working fluid. Equating the Reynolds number of the model and prototype ensures that the viscous and inertia forces are in the same proportion. For open channel flows, the hydraulic diameter is usually considered as the length scale. If the Reynolds number is kept constant for the model and the prototype, while using the same working fluid ($\rho_m = \rho_p$ and $\mu_m = \mu_p$),

the resulting velocity ratio would be inversely proportional to length scale ratio, as shown below.

$$\begin{aligned}
 Re_m &= Re_p \\
 \Rightarrow \frac{\rho_m V_m L_m}{\mu_m} &= \frac{\rho_p V_p L_p}{\mu_p} \\
 V_r &\propto \frac{1}{L_r} \tag{3.27}
 \end{aligned}$$

Based on the inlet hydraulic diameter and the inlet velocity, the Reynolds number is 6.7×10^5 and 1.4×10^5 for the higher and lower flow rates, respectively. Therefore, the inertial effects are prominent under the operating conditions considered in this study and the flow is in the fully turbulent region.

3.5.1.3 Weber Number

Weber number We represents the importance of inertia force over the surface tension force and it is defined as:

$$We = \frac{\rho L V^2}{\sigma} \tag{3.28}$$

where σ is the surface tension coefficient. Equating the Weber number ensures proportionality of surface tension and inertial forces. Usually for open channel flows, the inertia and gravitational forces are comparatively higher than the surface tension force. To get an idea of the relative magnitude of inertia force over the surface tension force for the reactor considered, the value of the Weber number is calculated below at the operating conditions.

The surface tension coefficient for the water-air interface at the room temperature is $0.076 [Nm^{-1}]$. Taking the length scale to be the width of the channel, which is $0.4064 [m]$, the velocity to be $1.1 [ms^{-1}]$ and the water density at room temperature $998.2 [kgm^{-3}]$, we get $We = 6458.7 \gg 1$. This suggests that the inertia force is

orders of magnitude higher than the surface tension force. Therefore, the Weber number similarity could be ignored for the scaling down requirement.

3.5.1.4 Relaxed Similitude Requirement

From Eqs. (3.25) and (3.27), it can be seen that when the same fluid is used in both model and prototype, maintaining both Froude and Reynolds number the same between the model and prototype is only possible if $L_r = 1$, i.e. model and the prototype are of the same size. Therefore, it is necessary to relax the similitude requirement. One way to do that is identifying forces that have important contribution and keeping corresponding force ratios the same.

Usually in open channel flows at high Reynolds number, the inertia force is much higher than the viscous force, whereas in the subcritical flow regime, the gravitational force is higher than the inertia force. So, the Froude number should be kept the same between the model and prototype. However, the Reynolds number for the model will be much lower than that for the prototype if keeping the Froude number the same. Since constant Froude number requires $V_r \propto \sqrt{L_r}$ which results in the Reynolds number for the model to be reduced by $Re_r = V_r L_r = L_r^{3/2}$. As an example, if the reactor is scaled down 10 times ($L_r = 0.1$), the Reynolds number for the model would be reduced by 32 times. The reduction in the Reynolds number for the model by one order of magnitude might make the viscous effect more significant. However, this decrease may not significantly affect the hydraulics and disinfection process in the reactor since the flow still remains in the turbulent regime.

Maintaining the Reynolds number constant will change the Froude number and consequently the flow regime. For a ten-times scaled down model, the constant Reynolds number will increase the Froude number from 0.45 (subcritical) to 14.23 (super-critical) under the operating conditions considered in this study, which would have significant impact on the flow characteristics and consequently the disinfection characteristics.

3.5.1.5 Maintaining Both Froude and Reynolds Numbers Constants

Both the Froude and the Reynolds numbers could be theoretically maintained constant by modifying the viscosity of the working fluid. Keeping the Froude number constant will reduce the Reynolds number by the ratio of $L_r^{3/2}$ if the same working fluid is used for both prototype and model. To make the Reynolds number the same, the dynamic viscosity μ of the working fluid has to be reduced by this ratio, while keeping the density same.

In this study, constant Froude number is first implemented numerically. Then, the viscosity of the working fluid is modified to maintain both the Froude number and the Reynolds number constants.

3.5.2 Similarity of the Radiation Field and the Disinfection Behaviour

In order to maintain the same microbial inactivation between the model and prototype reactors, it is necessary to have the same RED. Since the RED is a direct function of mean dose and the dose distribution, maintaining it constant would require the following:

1. The average dose remains the same.
2. The dose distribution remains the same.

Dose is defined as the integration of UV Intensity [$mWcm^{-2}$] over the residence time T [s] of the microbial particles. To maintain the average dose constant for the prototype and model reactors, the residence time ratio is calculated from the hydraulic similarity and the UV intensity ratio is updated accordingly. The details are discussed below:

- a) Given the length ratio is $L_r = 0.1$ then the mean velocity ratio would be $V_r = \sqrt{L_r} = \sqrt{0.1}$ for the same Froude number. Consequently, the mean residence time ratio would be $T_r = L_r/V_r = \sqrt{L_r}$ if the flow can be considered as a plug flow. However, if the fluid has a wider residence time distribution and the width of that distribution changes in the scaled down model, this scaling down technique would not result in similar disinfection behavior. In that case an average residence time

should be calculated from the distribution and that averaged value can be used for scaling down. In the results section, it will be shown that for the reactor under consideration, the residence time has a narrow distribution suggesting that the use of mean velocity ratio to calculate the residence time ratio is not that erroneous.

- b) To ensure the same dose, the UV intensity ratio (I_r) should be balanced accordingly, $I_r = 1/T_r = 1/\sqrt{L_r}$. That means the intensity has to be increased by $1/\sqrt{L_r}$ times. Care should be taken to decide which UV intensity value to use for the scaling down model. Since only the effect of radiation absorption is considered, the UV intensity distribution would follow the Beer-Lambert's law, which is self similar when normalized by the intensity at the lamp surface (I_0). This suggests that if the intensity at the lamp surface is scaled, the intensity within the whole domain would be scaled accordingly. However, if the free surface height in the scaled down system is not exactly similar to the full size one, this scaling down technique would include some errors in terms of the similarity in the radiation field. However, those errors can be taken care of by ensuring that the volume averaged intensities in both domains are scaled.

The distribution of the dose value would be similar if the spatial variation of the UV intensity in between the lamps is similar for both of the reactors. This requires the non-dimensional intensity (I/I_0) to be similar, which is possible if the quantity e^{-ax} is kept constant, where x is the distance between the lamps.

$$e^{-ax} = \text{constant}$$

$$\Rightarrow a_m * x_m = a_p * x_p$$

$$\Rightarrow \frac{a_m}{a_p} = \frac{x_p}{x_m} = \frac{1}{L_r} = 10 \quad (3.29)$$

The absorption coefficient of the fluid has to be increased 10 times in the scaled down model, leading to a decrease in the UVT of the fluid. For example, if $UVT_p = 60$ [%/cm], $a_p = 51.08$, so, $a_m = 510.8$ and $UVT_m = 0.60466$. This reduction in UVT

can be easily implemented by adding UVT modifier to the waste water, as making the fluid optically thicker is easier to accomplish than making it optically thinner.

Chapter 4

4 Results and Discussion

In this chapter, the grid sensitivity analysis will be performed and then the proposed CFD model will be validated against the available experimental data. The validated CFD model will be used to investigate the hydraulic and disinfection behavior of the reactor under different operating and geometrical conditions. The effects of the optical characteristics of the water and the UV sensitivity of different microbes on the disinfection performance will also be studied. A method to visually investigate the reactor behavior by identifying the low dosed particle trajectories will be presented. Then the hydrodynamic behavior and the effects of hydrodynamics on RED will be investigated for reactors with two lamp banks placed in series. At last, the validity of the developed scaling down methodology will be discussed by comparing the hydrodynamics and the disinfection behavior of the full size reactor and 10 times scaled down reactor.

4.1 Grid Independence Test

A grid sensitivity analysis is performed based on the predicted free surface height using different numbers of mesh elements for the highest flow rate of the reactor, which is 4320 gpm (US gallon per minute). The free surface height is chosen for the sensitivity analysis because of two reasons, 1) the free surface shape characterizes the hydraulic behavior of the open channel flow (i.e. subcritical/supercritical) and 2) the free surface shape especially in the lamp region affect the disinfection performance of the reactor as suggested by Peng et al. (2012). For a better comparison, the free surface height at every point is normalized based on its difference at the leading and the trailing edge of the lamp bank. At any point, the normalized water height can be mathematically expressed as $y_{norm} = (y - y_m)/(y_l - y_t)$, where y_m , y_l and y_t are the free surface height at the stream-wise midpoint, leading edge and the trailing edge of the lamp bank, respectively.

For both the reactors with or without the lamp support system, no lateral variation in the free surface height is found, which is shown in Figure 4.1 and Figure 4.2 for the reactors

without the lamp support and with the lamp support, respectively. Therefore, the free surface height at the lateral mid-plane is considered in the grid independent test.

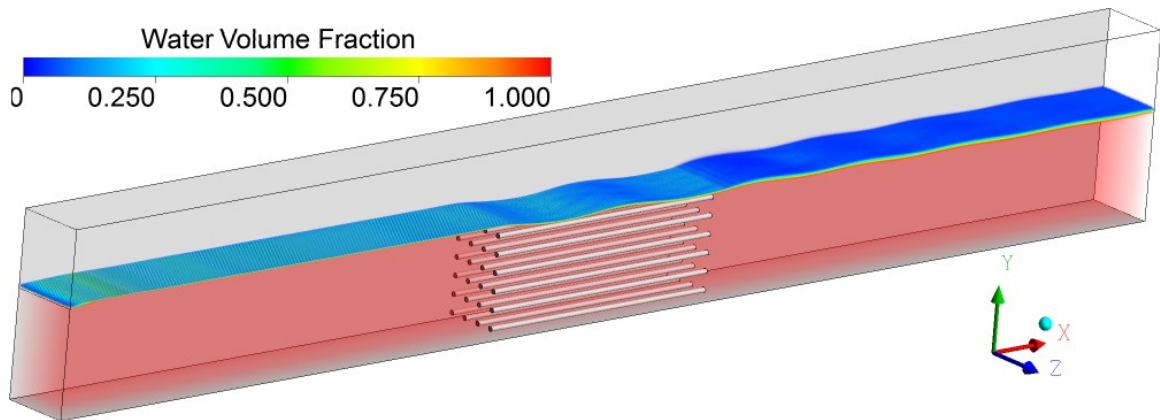


Figure 4.1 Free surface profile for the reactor without the lamp support

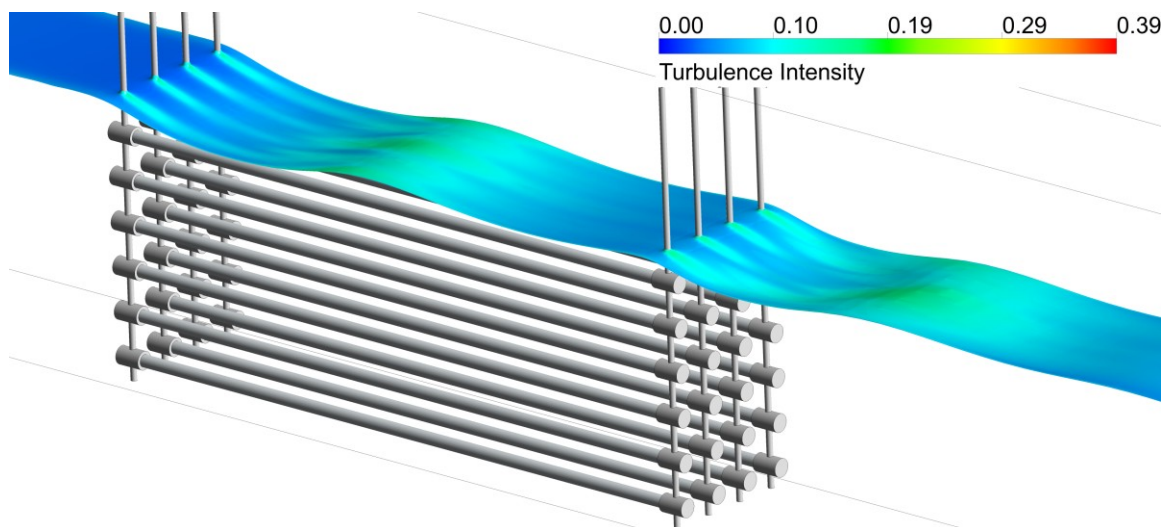


Figure 4.2 Free surface for the reactor with the lamp support

The free surface height for the reactor without the lamp support is shown in Figure 4.3 using different mesh sizes. It is found that the free surface profiles from the mesh with 4.87 million and 7.18 million elements are visually indistinguishable, which leads to the conclusion that the mesh having 4.87 million elements can give grid independent results and it is used for the rest of the simulations.

Two different grids with 4.9 million and 6.6 million hexahedral elements were used to determine the grid sensitivity of the reactor with the UV-lamp bank and the support assembly. Figure 4.4 indicates that both of these grids predict similar surface profiles, however, the grid having 6.6 million elements show surface waviness of higher amplitude. It was not possible to perform the simulation with a finer mesh for this geometry because of the high requirement of the computational resources. Therefore, this finer grid with 6.6 million is used.

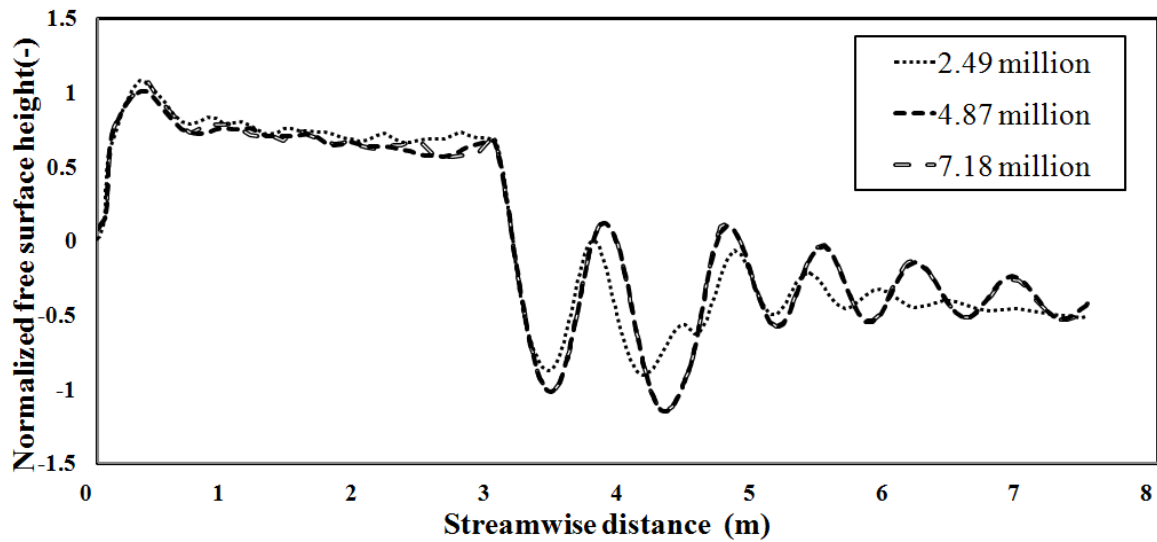


Figure 4.3 Comparison of the predicted normalized water level using different grid sizes for the reactor without the lamp support

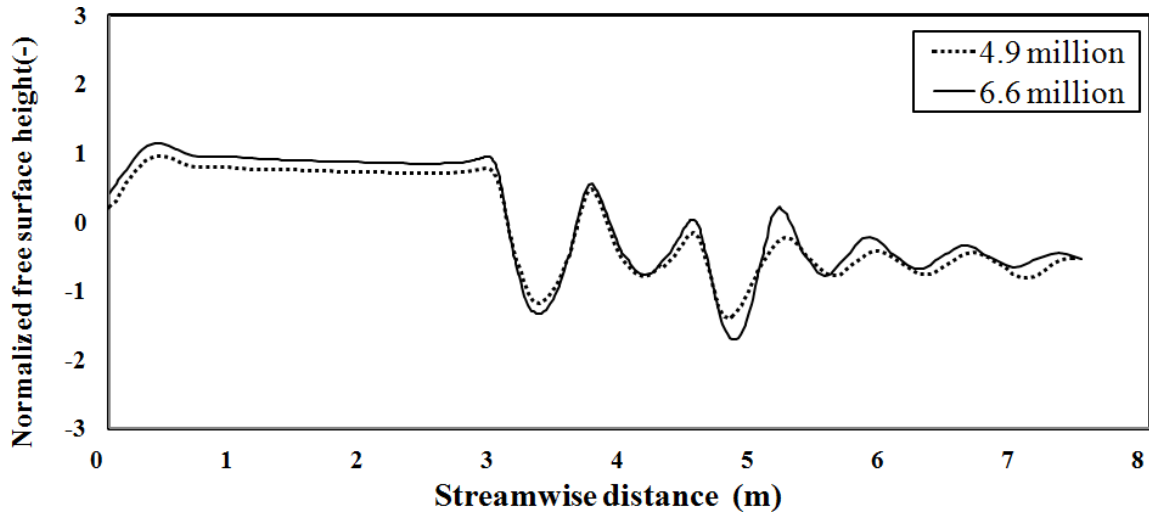


Figure 4.4 Comparison of the predicted normalized water level using different grid sizes for the reactor with the lamp support

4.2 CFD Model Validation

To validate the CFD model used in this work, the normalized free surface profile from the numerical simulation is compared with the experimental data for a full size reactor, which has all the geometrical details of a typical horizontal type open channel reactor (Peng et al., 2012). Figure 4.5 shows the comparison of the normalized free surface heights for both of the reactor models with the experimental data. It can be noticed that the free surface profiles for both reactor models qualitatively agree with the experimental data especially at the upstream of the channel and in the lamp region. The reactor model with the lamp support has better match with the experimental data compared to the reactor model without the lamp support. There exists a phase lag in the surface waviness between the two reactor models in the downstream of the lamps.

It should be noted that a time averaged solution without considering the transient behavior of the surface waves is reported in this work. Because of this as well as due to the elimination of all the complicated geometry features in the simulation, which potentially affect the free surface height, a qualitative agreement between simulation and experimental data is deemed to be satisfactory.

The comparison for the disinfection parameters is not made since the biological dosimetry data for this reactor are not available.

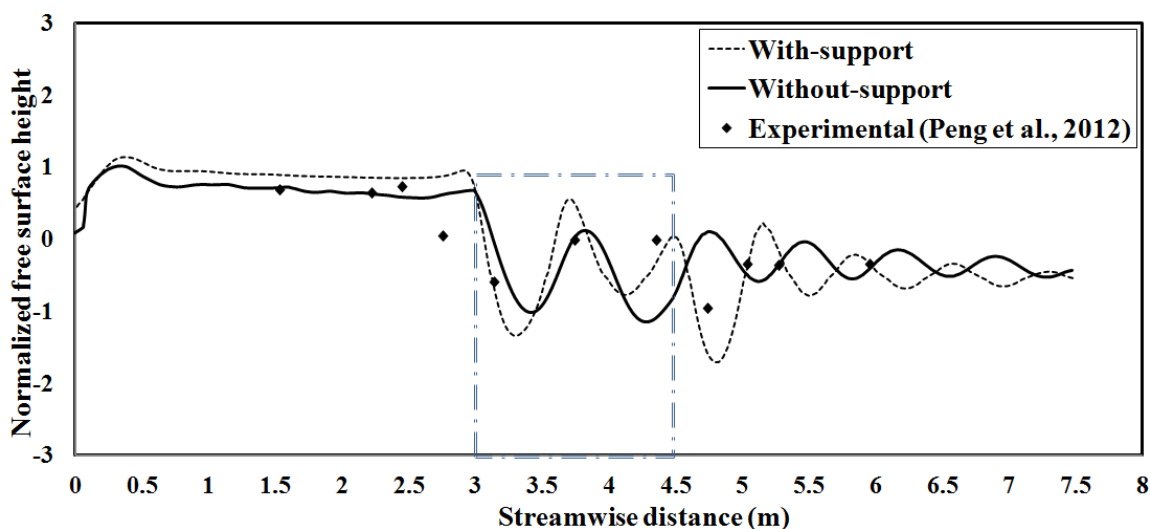


Figure 4.5 Comparison of the predicted normalized free surface height with the experimental data.

4.3 Effect of the Lamp Support Systems

It can be seen from Figure 4.5 that, both reactor models have qualitatively similar free surface profile in the lamp region. If the disinfection performances for both reactors are similar, the lamp support system could be neglected to reduce the computational cost.

Figure 4.6 shows the log removal achievable from both reactor models for microbes having different UV sensitivities. It can be noticed that achievable log removal is slightly higher in the reactor model without the lamp support than that with the lamp support. This might be attributed to the fact that for the reactor with the lamp support, the flow field is affected by the obstruction created by the lamp support, which causes more waviness in the free surface shape compared with the reactor without the lamp support.

The stream-wise velocity distribution at a horizontal plane passing through a lamp cross section is shown in Figure 4.7. It can be noticed that the water is deflected by the lamp support at the upstream of the channel and there is a small recirculation region immediately after that. This obstruction reduces the UV dose delivered by the lamps at

this region as water in this region bypasses the lamps and is not exposed to the high UV intensity region.

The qualitative disinfection performance is similar in both reactor models with or without the lamp support. Since the goal of this work is to qualitatively predict and compare the performance of the reactor under different conditions, this slight difference could be ignored for the benefit of reduced computational cost. Therefore, the subsequent analysis will be performed for the reactor without the lamp support system. This simplified reactor will provide insight on the importance of different parameters and theoretical details of the reactor.

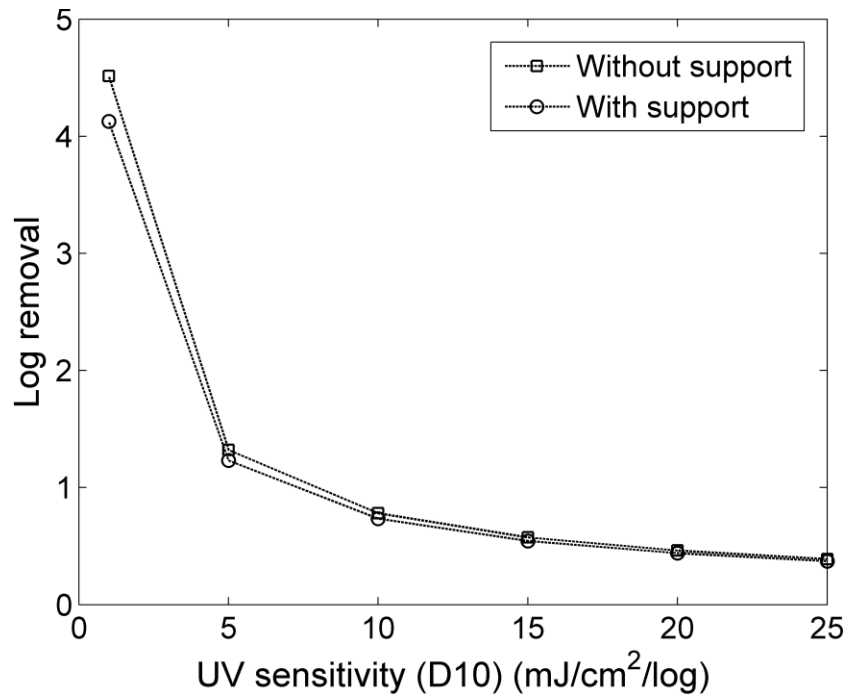


Figure 4.6 Log removal of the microorganism for both of the reactor models with and without the lamp support system

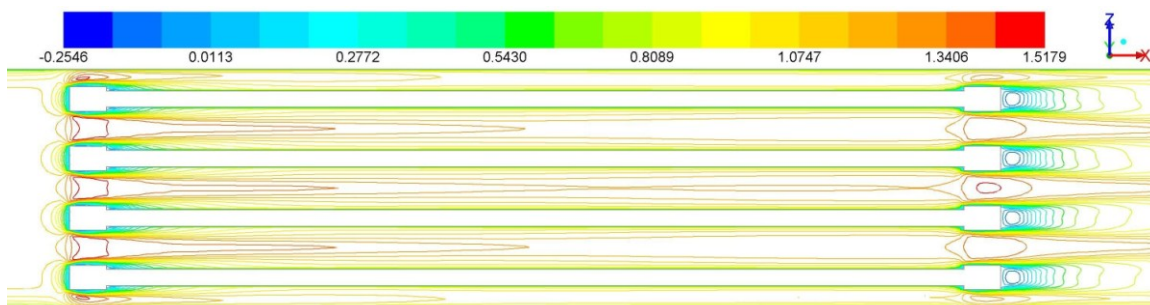


Figure 4.7 Stream-wise velocity contour (m/s) at a horizontal plane passing through a lamp cross section.

4.4 Existence of Secondary Current in the Reactor

Different researchers have reported that a secondary current may be produced in an open channel flow. This secondary current is the existence of a circular mean velocity field at a plane perpendicular to the stream-wise flow direction. This secondary current is manifested by the velocity dip phenomena, which is the existence of the maximum stream-wise velocity at a point lower than the free surface. Nezu et al. (1989) reported that a narrow channel having a width to depth ratio less than 5 usually exhibits this phenomenon. Considering the width to average depth ratio of the reactor being studied is 0.67, a secondary current may be expected.

For straight open channels having rectangular cross section, this secondary current is produced due to the anisotropy in turbulence (Nezu et al., 1993). Since the $k - \epsilon$ turbulence model assumes isotropic turbulence, it cannot produce this secondary current in an open channel. To capture any secondary current that might exist in the reactors, the Reynolds stress model (RSM) is used since RSM does not assume isotropic turbulence and solves for all six Reynolds stress components.

The free surfaces predicted by both the RSM and $k - \epsilon$ turbulence models are shown in Figure 4.8. It can be noticed that both RSM and $k - \epsilon$ models predict the same free surface profile. However, RSM predicts slight more fluctuations in the free surface shape at the upstream of the channel.

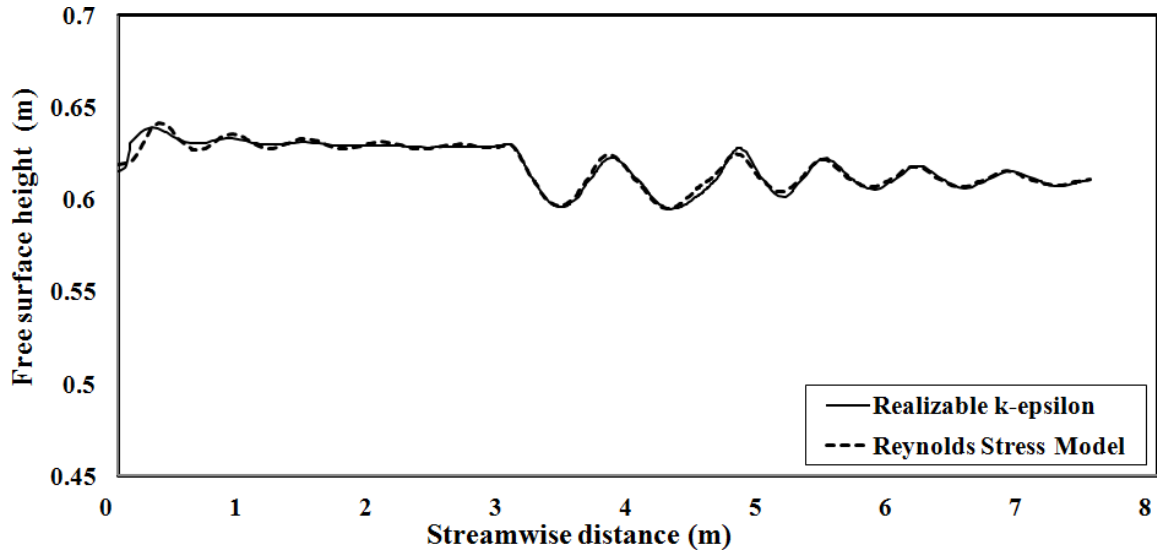


Figure 4.8 Free surface height predicted by $k - \epsilon$ and RSM turbulence model

To identify the secondary current, a vertical plane at 0.5 m upstream of the lamp bank is chosen. The easiest method would be to plot the velocity vector with in-plane velocity components (i.e. V_y and V_z) on this plane and visually identify any circular motion. However, for secondary currents of very small magnitude, this method is not effective. Therefore rather than identifying the secondary current, identification of the velocity dip phenomena which is a direct result of secondary current would be easier (Nezu and Nakagawa, 1984). The velocity dip phenomena should be easily noticed from the iso-lines of stream-wise velocity contour as a circular or elliptical shape just below the free surface. Figure 4.9 shows the velocity contour on the selected plane for both water and air phases using RSM turbulence model, which suggests no secondary current in the reactors considered.

To further validate whether the secondary current exists in the reactor, the shear stress at the bottom wall on this selected plane is plotted in Figure 4.10. If there is any secondary current or velocity dip phenomenon, the bottom shear stress should exhibit a local minima or maxima at the channel centerline (Nezu and Nakagawa, 1984). No such feature is observed from this figure. The little bumps in the shear stress profile, which is produced by both $k - \epsilon$ and RSM models are believed to be produced as a result of the velocity field being affected by the presence of the lamps downstream.

It can be concluded that no secondary current is produced in the reactor under the current flow situation. This allows the use of $k - \epsilon$ model for further numerical study of the reactor. Therefore, the results reported in the following sections are from the $k - \epsilon$ turbulence model to reduce the computational time.

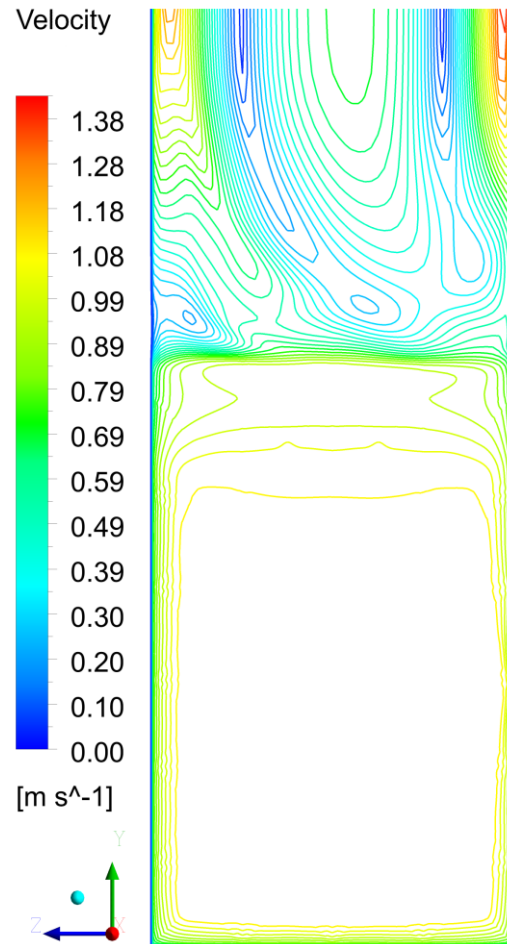


Figure 4.9 Iso-lines of stream-wise velocity magnitude at 0.5 m upstream of the lamp bank

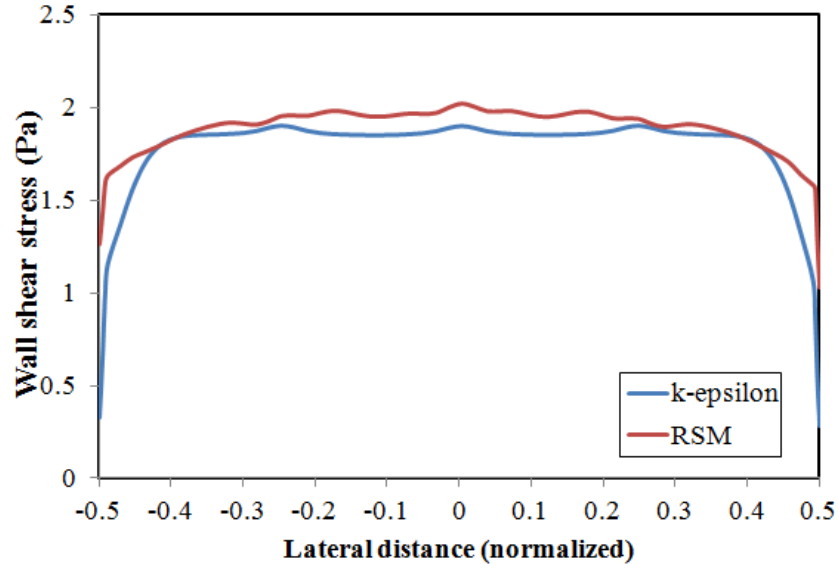


Figure 4.10 Wall shear stress at 0.5m upstream of lamp bank

4.5 Parametric Analysis

A parametric study is performed in this section to understand the effect of different operation parameters on the performance of the reactor. The effects of flow rate, optical quality of the water to be disinfected and the UV sensitivity of the target microbes are considered. The effect of these parameters on both the reactor hydrodynamics and the disinfection performance is discussed in detail.

4.5.1 Effect of the Flow Rate on the Free Surface Profile

The reactor is simulated under three different flow rates (4320, 2617 and 914 gpm). Figure 4.11 shows the free surface levels at different flow rates. The figure show that the free surface height increases with the flow rate at the upstream of the channel since the flow is entirely in the subcritical range and the downstream conditions may affect the upstream in this range. Since the computational model is setup to ensure the free surface height to be 0.6096 [m] at the channel outlet to mimic the height control system used in the actual reactor, the drop in total energy head is balanced by the increase in free surface height at the upstream section.

At higher flow rate, i.e., at higher flow velocity, the free surface shows more waviness, which is due to higher Froude number ($Fr=0.45$). At a lower flow rate, the Froude number is low ($Fr=0.095$), therefore, the influence of gravitational force is high enough compared to the inertial force to smooth out any disturbance. At the high flow rate, the obstructions created by the lamp bank produce high amplitude surface waves due to the increased influence of inertia. It should be noted here that the surface waves of small amplitudes are not captured by the solver since it is a steady state solution.

The static pressure at the midline along the bottom wall is plotted in Figure 4.12. It can be noticed that the pressure decreases along the reactor. The gradual decrease in the static pressure at the channel upstream region is due to the frictional loss at the walls. The abrupt pressure decrease at the beginning of the lamp bank is due to the increase in velocity in that region as a result of a decreased cross sectional area. The frictional loss in the lamp region is very high because of the presence of lamps. At the end of the lamp bank, the pressure is partially recovered due to the increase in the cross sectional area and then continues to decrease in the downstream due to wall shear.

The decrease in the static pressure varies significantly with the flow rate. For the high, medium and low flow rate cases, the losses in pressure head are 234 Pa, 73 Pa and 24 Pa, respectively. The conventional specific energy approach which neglects the frictional losses at the wall cannot predict the pressure loss. This multiphase VOF model along with the turbulence model utilized in this work can however predict the frictional losses by calculating the shear stress at the wall. Since the shear stress increases with the increase in the velocity the pressure loss increases accordingly. This method can be used to predict the pressure head required to sustain the flow.

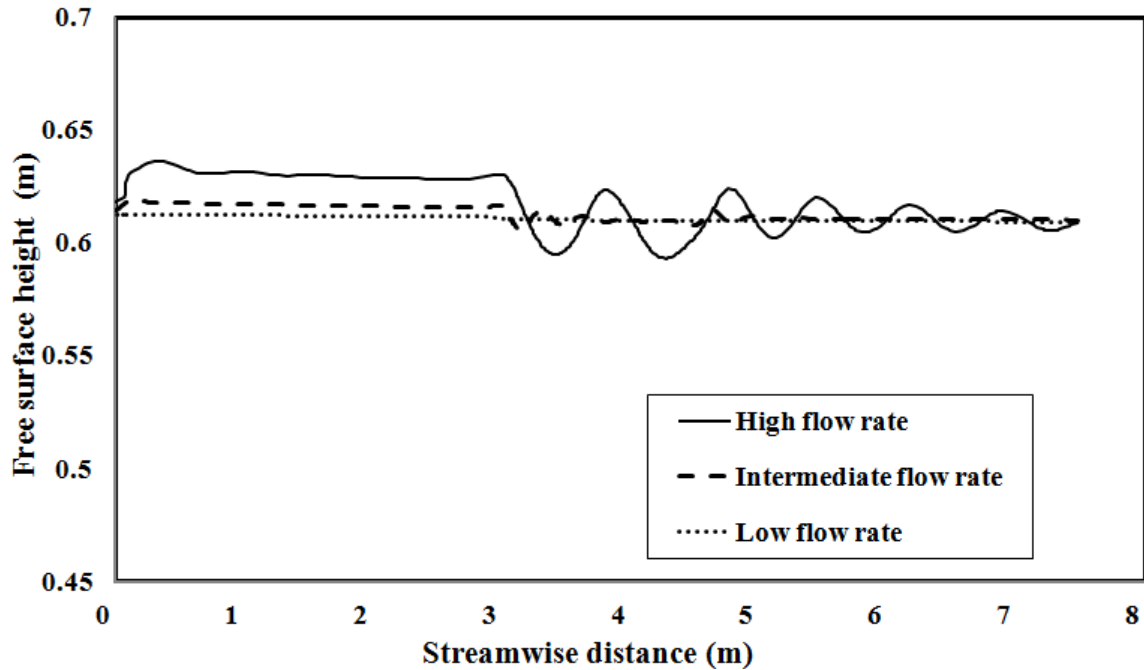


Figure 4.11 Comparison of the absolute free surface heights at different flow rates.

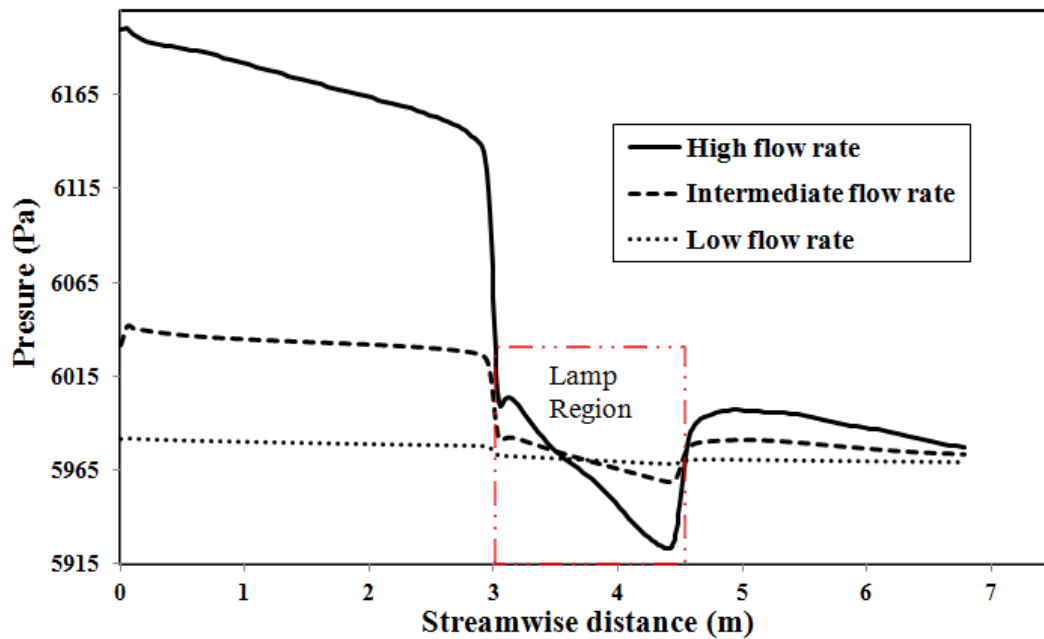


Figure 4.12 Comparison of the pressure head losses within the reactor at different flow rates.

4.5.2 Effect of Flow Rate and UV Sensitivity of the Microbes on the Disinfection Performance

The velocity of the fluid has significant effect on the disinfection performance of the reactor. The UV sensitivity of the microbes governs the achievable log removal from the reactor. Therefore, the quantitative effect of the flow rate and UV sensitivity of different microbial species on the reactor disinfection performance needs to be investigated. The UVT value of 60 ($\%/cm$) is considered since the secondary effluent in wastewater treatment plants usually has UVT value in the range of 45 to 70 ($\%/cm$) (Asano, 2007). Figure 4.13 shows the achievable log removal and RED from the reactor under different flow rates and different microbial species in terms of different d_{10} values. It can be easily noticed that for the lower flow rate, the log removal is always higher than that at the higher flow rate. This is simply because a lower fluid velocity results in an increase in the residence time of the microbes which facilitates to higher UV dose delivered and consequently results in higher log removal. The achievable log removal decreases with the increase in d_{10} . This is due to the fact that the microbes are much more resistant to the UV radiation if they have a high d_{10} value (dosage required for 1-log removal). The RED value increases with the d_{10} value since higher dosages are required to achieve the same log removal for microbes with high d_{10} values.

It can be noticed that the difference in log removal between the high flow rate and low flow rate decreases with the increase in the d_{10} value. This can be explained using the probability density function (PDF) of the dosage, which illustrates its distribution on the particles, as shown in Figure 4.14. It can be observed that the probabilistic peak occurs at around $5 \text{ mJ}/\text{cm}^2$ and $25 \text{ mJ}/\text{cm}^2$ dose values for high and low flow rates, respectively. This is expected, as the mean dose on the particles should be higher in the low flow rate case because of higher residence time. This positive shift in peak dose value suggests that the microbes having low d_{10} values will have significantly higher dosage in the low flow rate compared to the high flow rate. However, the microbes having higher d_{10} values do not have much improvement in log removal due to this shift just because being highly insensitive to UV exposure. It is also observed from the PDFs that for the low flow rate condition the probability of occurrence at the low dose region is qualitatively different

from that in high flow rate. This will also affect the log removal for highly sensitive microbes as they are much affected by the low dose region of the PDF.

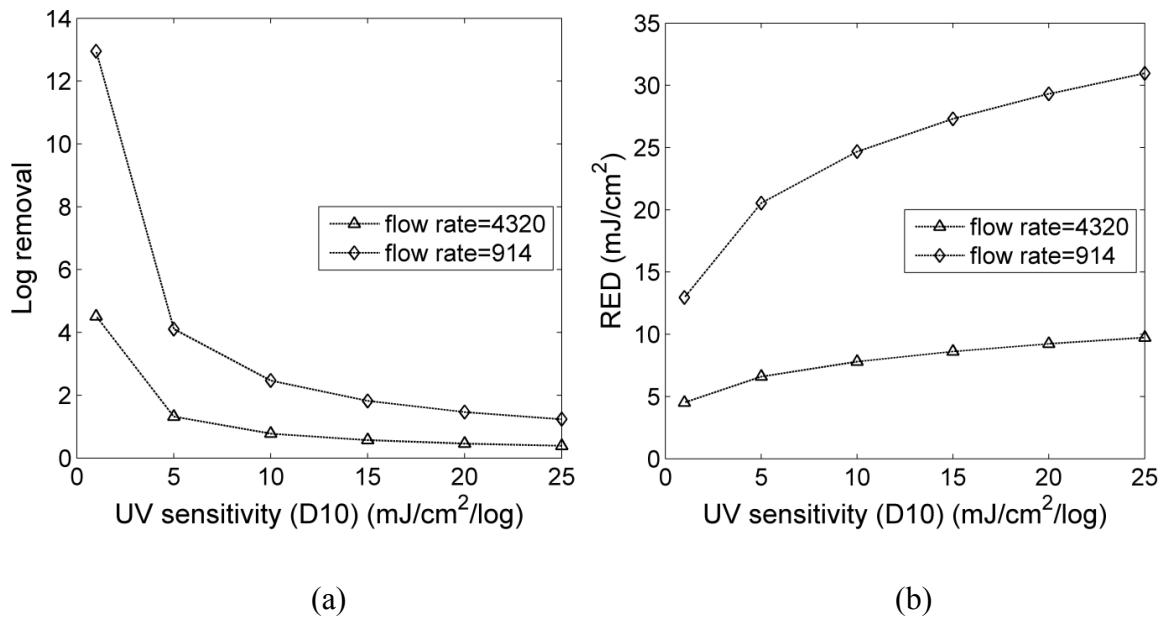


Figure 4.13 Log removal and the obtainable RED at different flow rates.

(a) Log removal and (b) RED

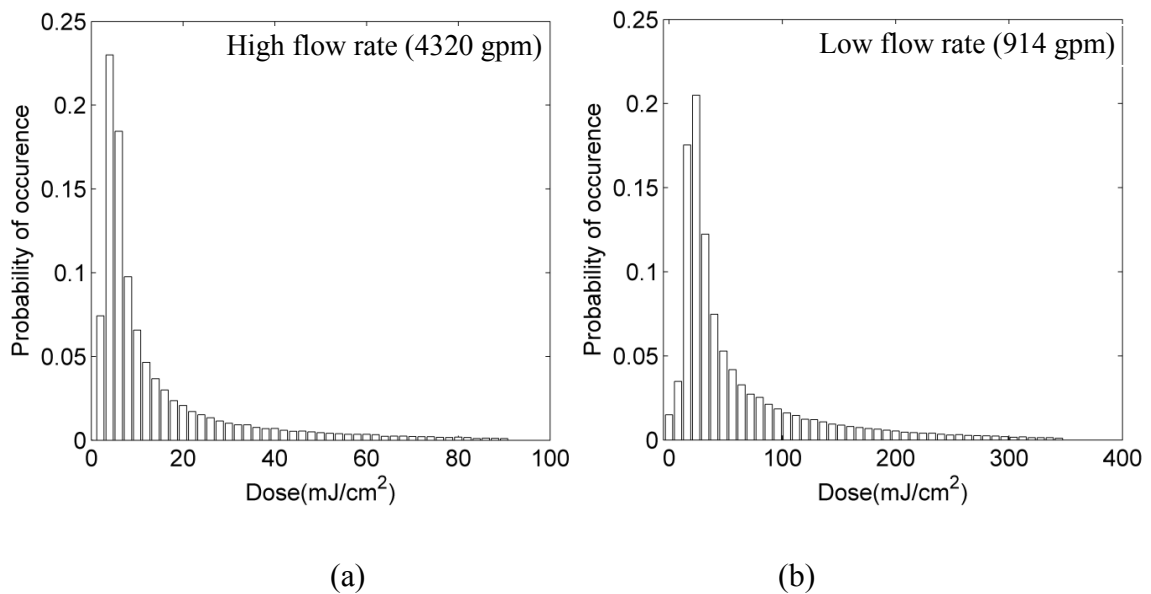


Figure 4.14 Probability density function of UV dose

An important aspect of the flow field affecting the log inactivation is the development of the boundary layer profile around the lamps. To illustrate this, the stream-wise velocities at a horizontal line passing through the mid-stream-wise plane and the third lamp from the bottom are plotted in Figure 4.15. It can be noticed that the boundary layer thickness is greater in the low flow rate case as the viscous effect becomes more important at lower Reynolds number. This thicker boundary layer around the lamp for low flow rate condition increases the residence time of the microbial particles flowing around the vicinity of the lamps. Since the UV intensity is also significantly higher in the region near the lamps, those low velocity particles are exposed to high UV intensity leading to a high dosage. However, in the high flow rate condition, the boundary layer is thinner, therefore, this effect is less important.

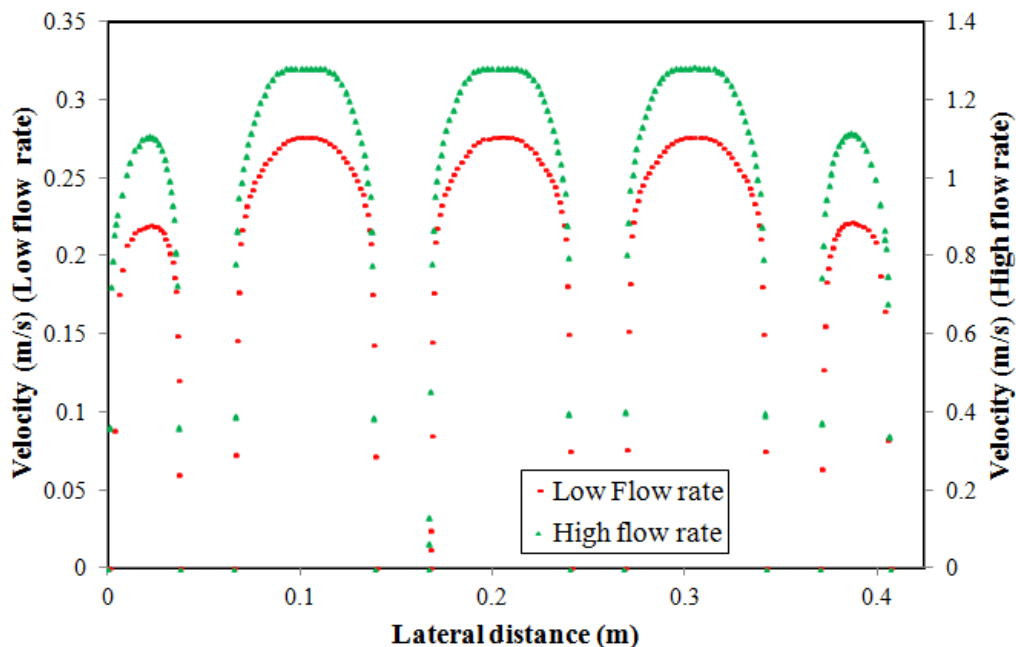


Figure 4.15 Stream-wise velocity profile at the mid stream-wise cross section passing through the lamp

4.5.3 Effect of the Water UVT on the Disinfection Performance

As expected, the UV transmittance of the water has significant effect on the disinfection performance of the reactor. Figure 4.16 shows the log removal for three different UVT values, which are typical values in wastewater treatment plants. It can be noticed that the

log removal increases with the increase in the UVT. It can also be noticed that the gap between the log removal curves at different UVTs decreases with the increase in D_{10} values of the microbes for both high and low flow rates. This suggests that the improvement of the disinfection performance of the reactor for highly UV insensitive microbes will not be significant by improving the optical properties of the water. This is mainly due to the fact that the UV intensity decreases exponentially from the lamp sleeves as shown in Figure 4.17. Highly UV insensitive microbes are probably disinfected in the region very close to the lamps. Increasing the UVT of the water extends this particular disinfection region only slightly, thus leading to little improvement in their disinfection process. Therefore, increasing the optical qualities of the water will not suffice to improve the disinfection performance for highly UV insensitive microbes, rather the distance between the lamps and between the lamp and the channel wall can be reduced in order to achieve that. That might come with an expense of additional pressure drop due to the compact packing of the lamps in a bank.

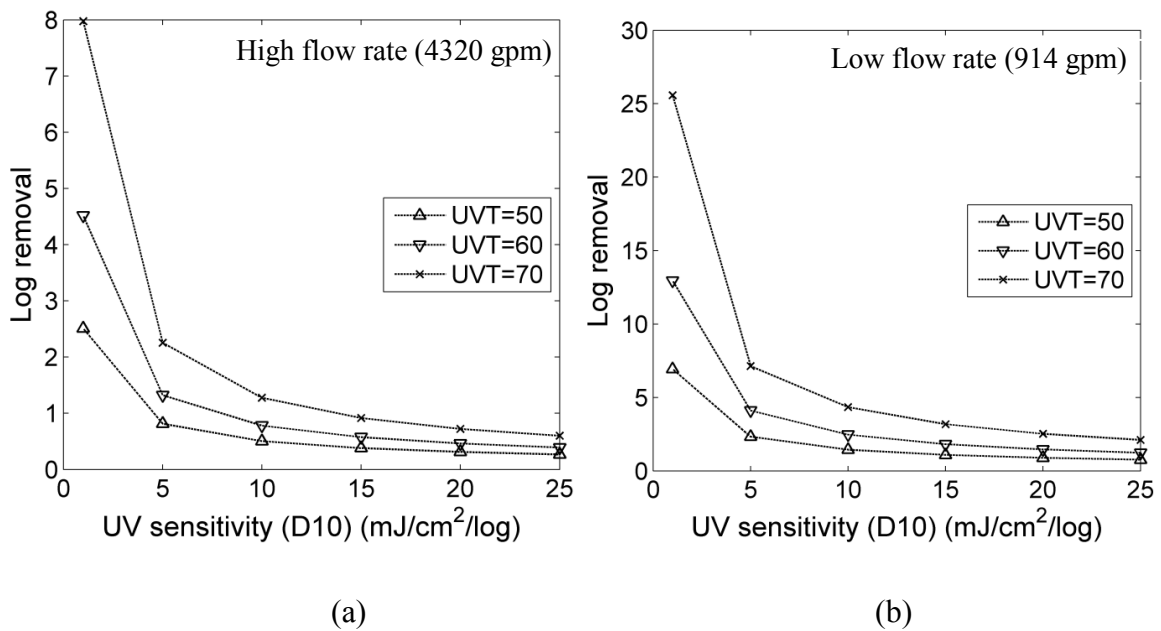


Figure 4.16 Variation of achievable log-removal with water UVT

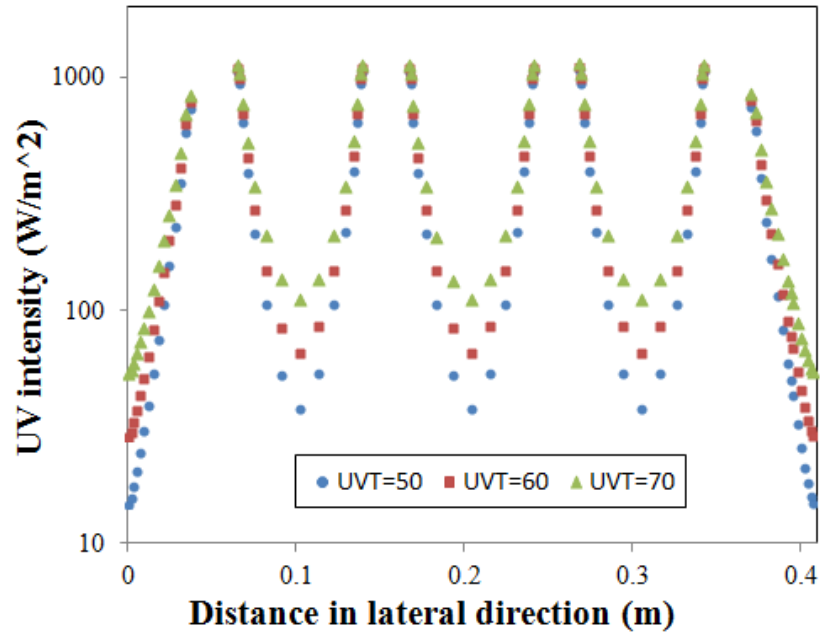


Figure 4.17 UV intensity distribution around the lamps along a horizontal line for different UVT values.

4.6 Visualization of the UV Radiation Intensity Distribution and Particle Doses

Low dosed particles are the reason for poor disinfection performance of the reactor. Effective visualization techniques are developed in this study to identify those within the domain. The trajectories of the particles having dose value less than $30 \text{ (mJ/cm}^2\text{)}$ are plotted in Figure 4.18 along with the volume rendering of UV radiation intensity. This numerical value of dose is randomly chosen for a particular disinfection process to separate out particle trajectories and should not be taken as an indication of low dose. A qualitative idea of the whole disinfection process within the reactor can be seen from this figure. As expected, it can be seen that low dose particles are traveling within the gaps between the lamps where the UV intensity is low, and near the free surface because of the waviness termed as the free surface effect by Peng et al. (2012).

To identify the microbial particles which are getting a low dose, a user defined function is developed in ANSYS FLUENT. The particle IDs of those trajectories are captured at the outlet of the reactor and the trajectory data are exported to ANSYS CFD-post software

for visualization. This technique can be used to visually examine the reactor behavior for subsequent design improvement.

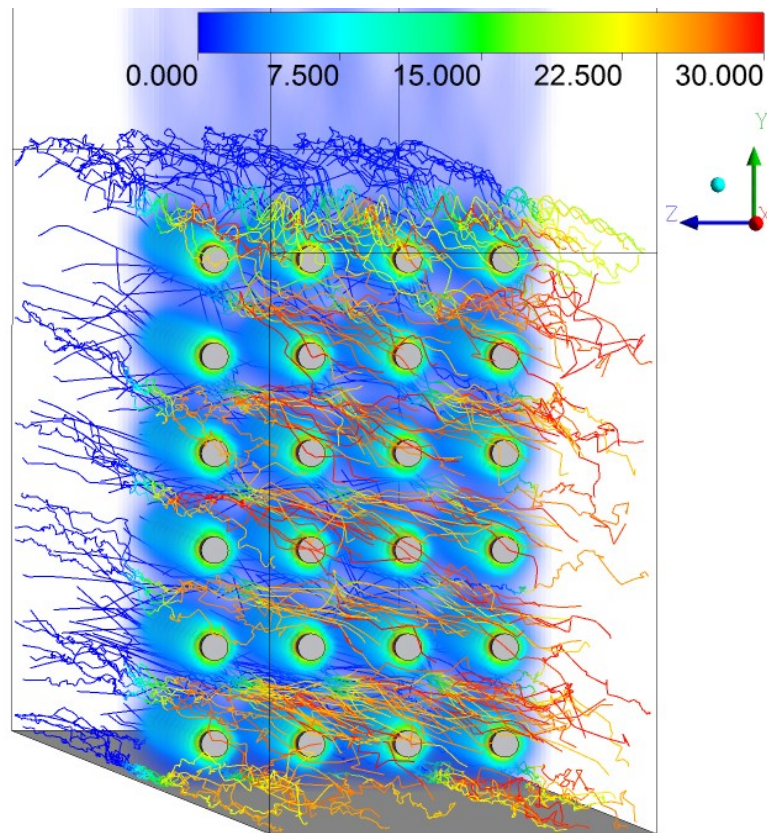


Figure 4.18 Low dosed particle trajectories colored by the dose value (ranging from 0 to 30 mJ/cm^2).

4.7 Reactors with Two Lamp Banks

In this section, the hydrodynamic and disinfection behaviors of the reactor having two lamp banks placed in series are discussed. Of particular interest is the additive behavior of RED for this type of reactors.

The stream-wise distance between the two lamp banks placed in series is taken to be the same as the length of the individual lamp bank. The second lamp bank does not have any lateral or vertical offset with reference to the first one. Three different geometric configurations are considered for the shape of the section of the channel between the lamp banks (which is termed as joint): 1) straight joint, 2) constricted joint with V type

constriction (25% reduction at the half-width) and 3) expanded joint with V type expansion (50% increase at the half-width). For all these three cases, structured hexahedral meshes are generated. The number of mesh elements required for these cases would increase up to 10 million or higher, which is prohibitive due to the limitation of the computational resources. Since the geometry under consideration is symmetric with respect to the lateral mid-plane, it would be highly beneficial in terms of the computational cost to consider the half of the geometry. A closer observation is made on the solution field in a reactor having only one lamp bank. Figure 4.19 shows the stream-wise velocity and the turbulence intensity at a vertical cross-section at the mid-stream-wise distance. It is interesting to notice that both the velocity field and the turbulence intensity are symmetric with reference to the lateral mid-plane. The symmetry of the velocity field can be further verified from Figure 4.15, which clearly shows the gradient of velocity field at the lateral mid point is zero for both high and low flow rate. Based on these observations, the flow in the reactor can be considered symmetrical. Therefore, the simulations for the reactors having two lamp banks are carried out only for half of the geometry with the symmetry boundary condition imposed at the lateral mid-plane.

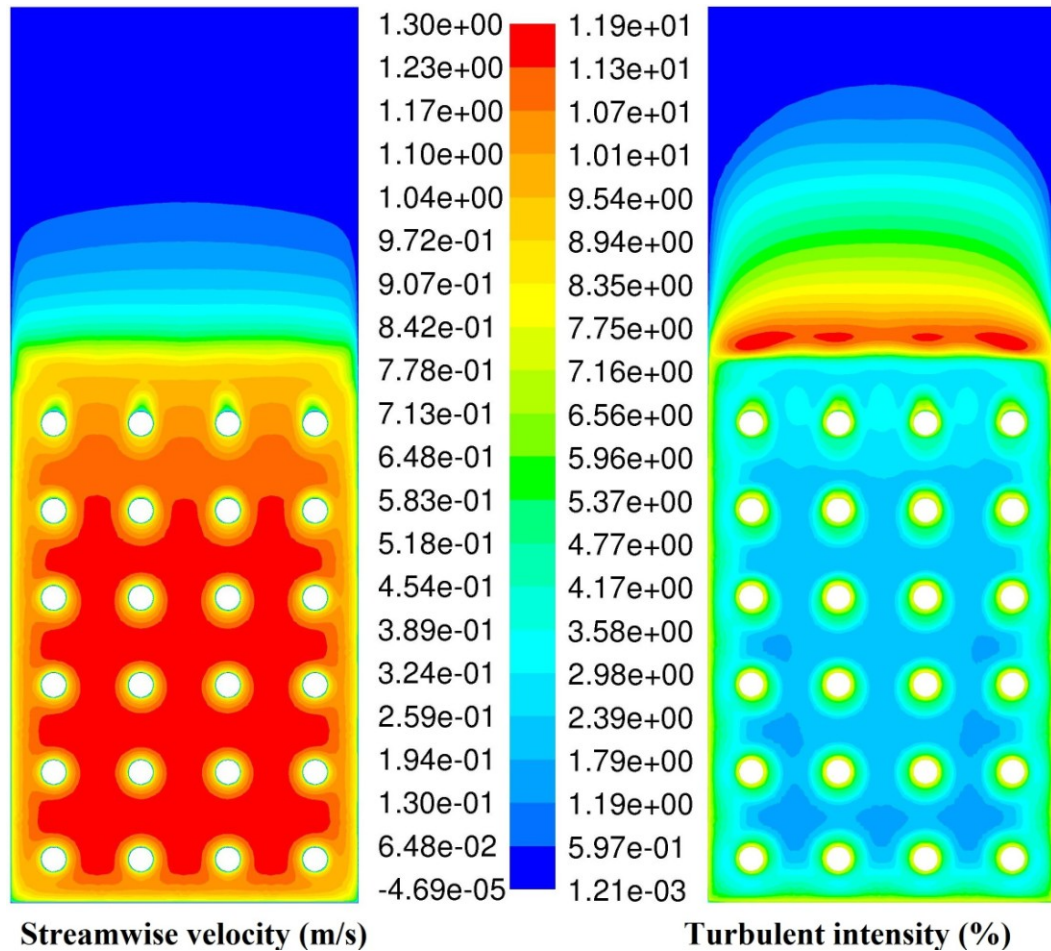
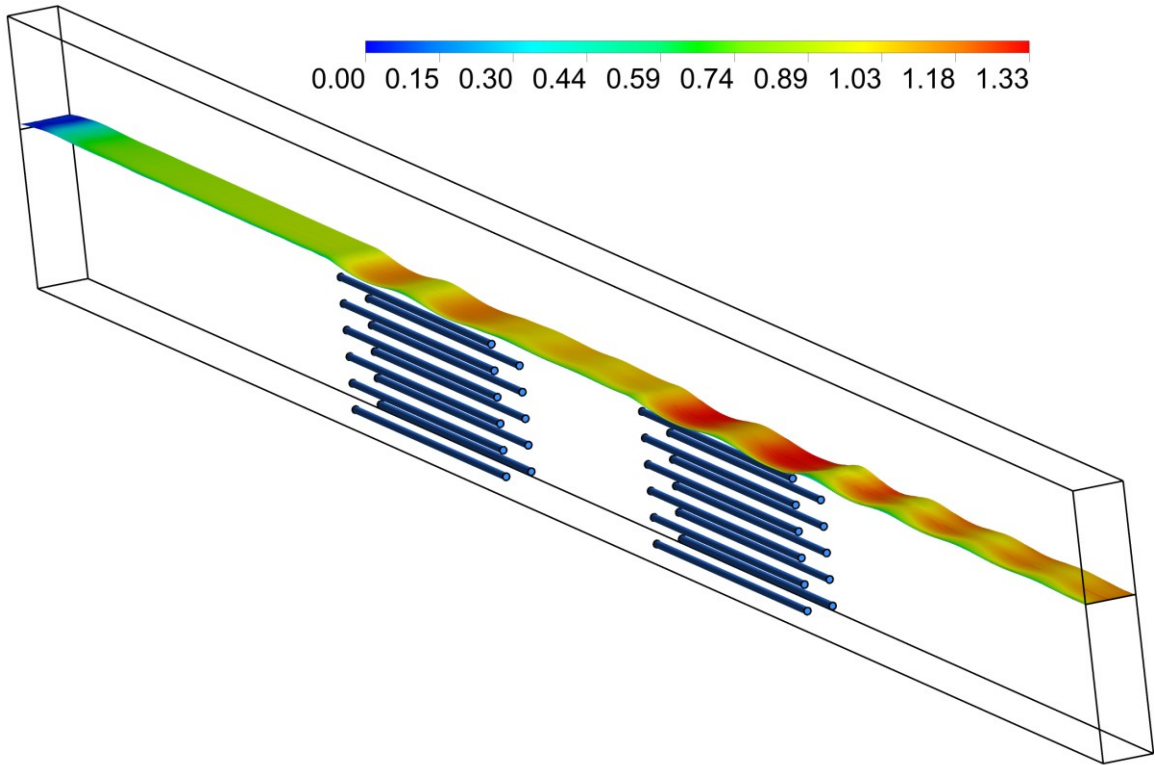


Figure 4.19 Stream-wise velocity and turbulence intensity at mid-stream-wise plane

4.7.1 Hydrodynamic Behaviour in the Reactor with Two Lamp Banks

The free surface profiles for the two-bank reactors with straight joint, expanded joint and the constricted joint are shown in Figure 4.20, Figure 4.21 and Figure 4.22, respectively for the high flow rate case (4320 gpm). In all these figures, the free surface is colored with the velocity magnitude to better show the surface waviness, as the higher velocity magnitude suggests that there is a dip in the free surface. The free surface characteristics of these reactors can be observed at a glance from these three figures. It can be quickly noticed that the water depth in the joint section between the lamp banks is increased for the expanded joint and decreased for the constricted joint. For the constricted joint, there also exists a recirculation region at the upstream of the second bank.



**Figure 4.20 Free surface profile for the two-bank reactor having straight joint
(colored with velocity magnitude m/s)**

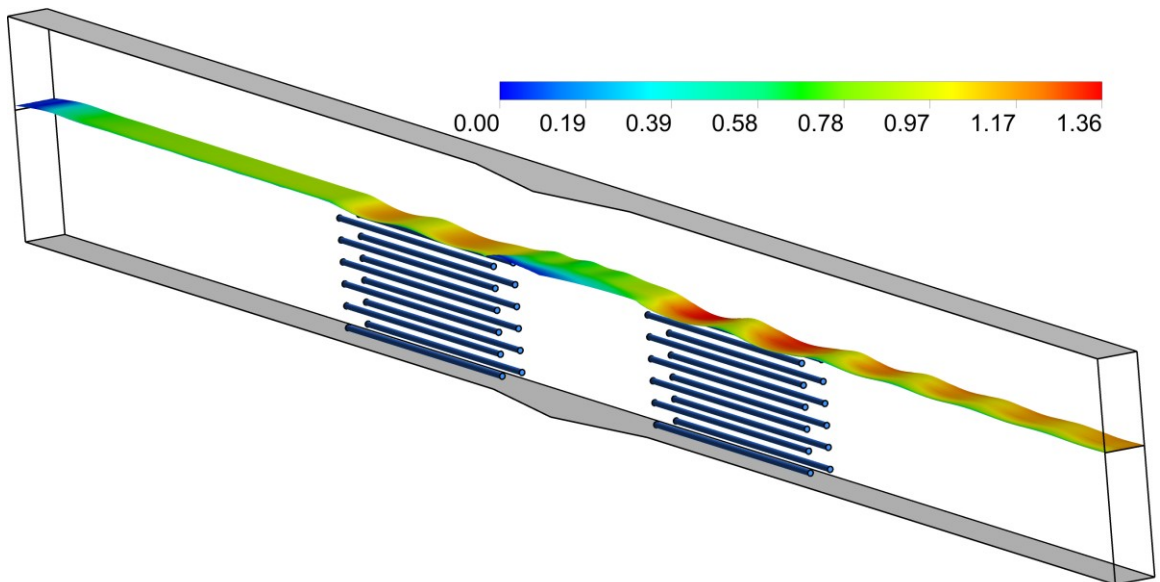


**Figure 4.21 Free surface profile for the two-bank reactor having expanded joint
(colored with velocity magnitude m/s)**

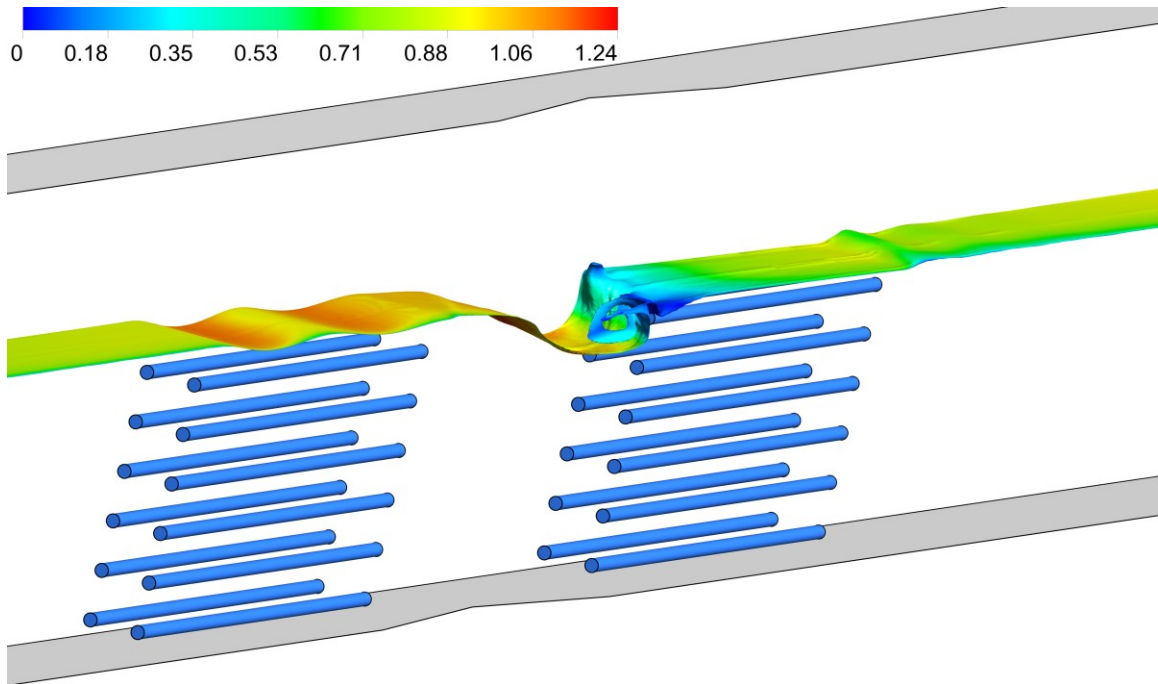


Figure 4.22 Free surface profile for the two-bank reactor having constricted joint (colored with velocity magnitude m/s)

For a future investigation of the hydrodynamic behavior of these three reactors, the free surface heights at the symmetry boundary are plotted in Figure 4.23. It is clear that for the reactors having straight and expanded joints the flow depths are exactly similar till the downstream point of the first lamp bank. However for the expanded joint the flow depth suddenly increases at the joint section and in the second lamp bank region the flow depth have similar oscillation compared to the straight joint case. The flow depth in the constricted joint gradually decreases within the whole joint section and suddenly increases just immediately before the second lamp bank.

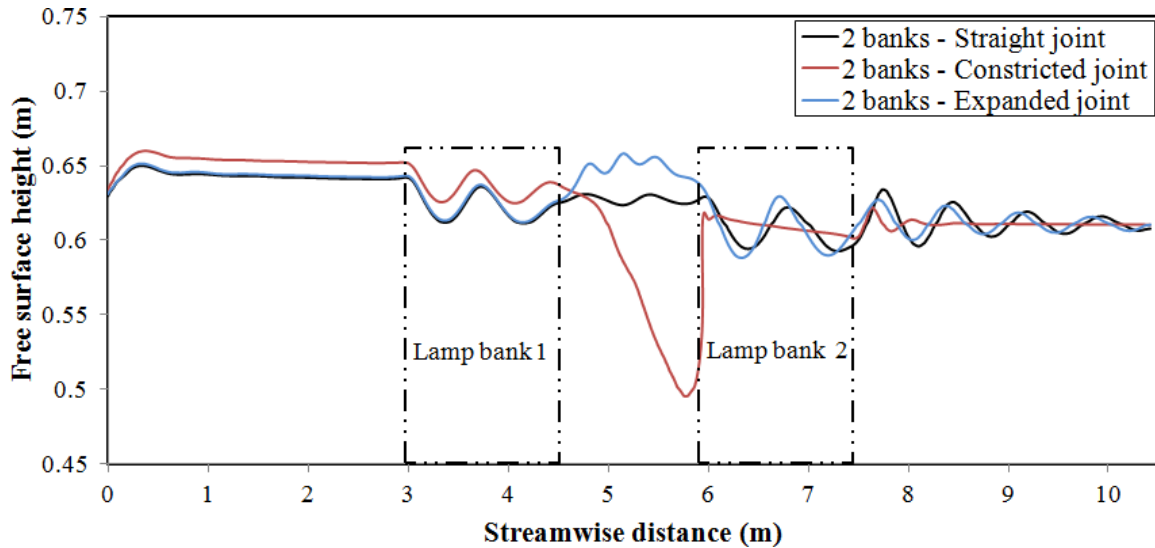


Figure 4.23 Comparison of the free surface heights for the two-bank reactors having different joints

The reason that the flow depth decreases in the constricted channel and increases in the expanded channel can be explained using the conventional specific energy concept in open channel flows. The total energy head H is the total energy (kinetic + potential + pressure) per unit weight of the fluid and can be expressed as:

$$H = \frac{V^2}{2g} + y + \frac{P}{\gamma}$$

where V represents the mean fluid velocity and y represents the flow depth. γ is the specific weight of the liquid. For an open channel having a zero bed slope, the pressure loss between two different points at the stream-wise direction can be ignored if the frictional effects are ignored. Considering an open channel having rectangular cross section with unit width and denoting the flow rate per unit width as $q (= y * V)$, the total energy head H can be expressed as:

$$H = \frac{q^2}{2gy^2} + y$$

This equation is known as the energy head versus depth relation. The quadratic nature of the equation in terms of y suggests that there exist two different y values at the same H

for the fluid. This is shown in Figure 4.24 as the alternate depth line (green line) for the operating conditions of the reactor considered. In this figure the black $H - y$ curve is plotted based on the q value (flow rate per unit width) in the reactor having the straight joint. Another two lines are plotted based on the q values for the constricted and the expanded channels. It should be noted here that since the flow rate should be conserved at every cross section, the flow rate per unit width at the joint will decrease for the expanded joint and increase for the constricted joint.

The red line indicates the critical flow condition and the flow above this red line is termed as sub-critical flow, whereas the lower section is termed as supercritical flow. The alternate depth line (green in color) is a constant energy line. Therefore, all the points on this line represent the same energy of the fluid. If we consider that the energy (H) at the constricted section is the same as the energy at a regular cross section, point a and point c in Figure 4.24 would represent the flow depths at the regular and the constricted sections, respectively. It is easily noticeable that the flow depth corresponding to point c is lower than the flow depth corresponding to point a , suggesting that at the constriction channel the flow depth should decrease if there are no losses ($H = \text{constant}$). Similar reasoning can be applied for the points a and e to show that at the expansion channel the flow depth would increase at the subcritical flow region.

The decrease or increase of the flow depth predicted by these curves is not quantitatively correct as it assumes there are no losses and also the alternate depth line is drawn considering the free surface height at the immediate upstream of the joint is 0.6096 m, which is not exactly the case. It can be concluded that the variation in flow depth predicted by the VOF solver is in well agreement with the conventional specific energy concept in open channel flow. Since the multiphase model utilized in this work incorporates the frictional losses which is manifested by the loss in pressure head, the variation in flow depth calculated should be more accurate.

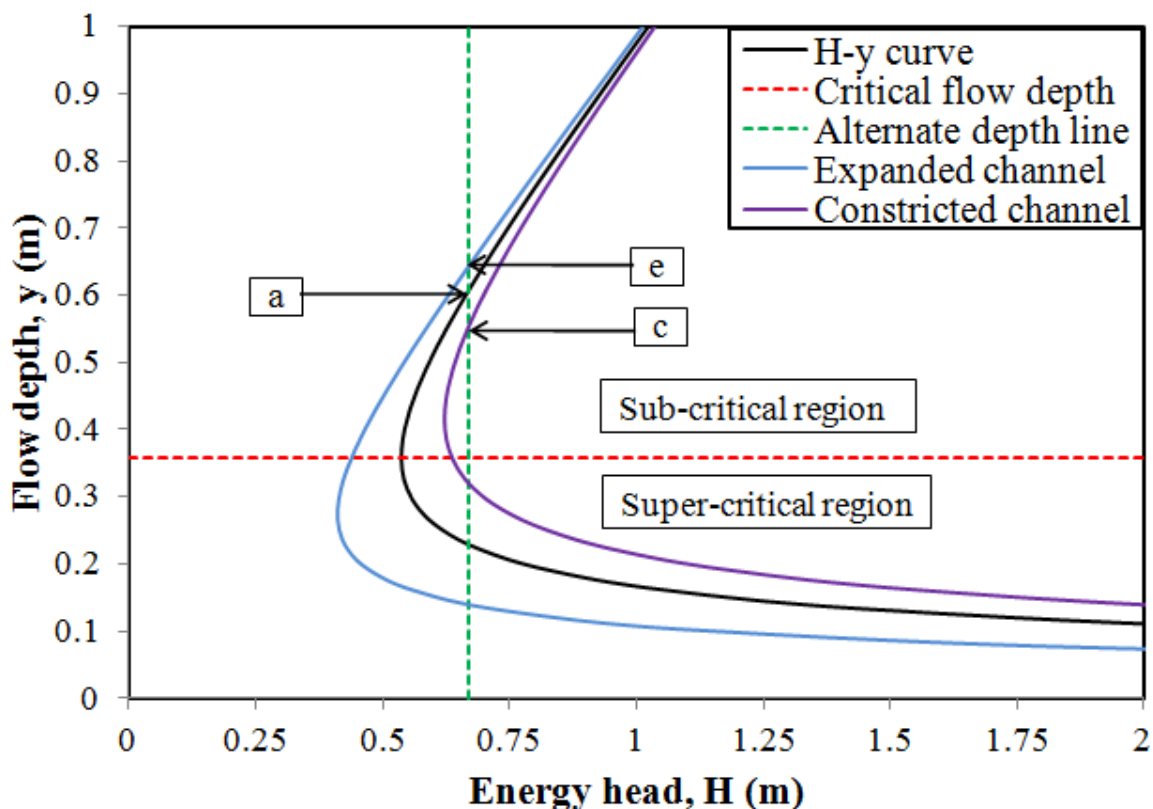


Figure 4.24 Energy-depth curve

4.7.2 Disinfection Behaviour in the Reactors with Two Lamp Banks

The particular attention in this section is on the additive nature of the RED in the reactors due to addition of the second bank. The RED for the three reactors having two lamp banks are plotted along with twice the RED achievable from the reactor having one bank. It can be noticed that for all the reactors having two lamp banks the achievable RED is lower than twice the RED of reactor having one bank. The constricted joint has the highest positive impact on the RED increase, which is probably due to the decreased flow depth and velocity at the second bank section. The expanded joint has more positive impact on RED increase compared to the straight joint. The quantitative values of the RED increase are summarized in Table 4.1 in terms of the multiplication factor (M. F.). This multiplication factor quantifies the ratio of the RED of the reactors having two lamp banks with respect to that in the reactor having only one bank at the same flow condition and the UV sensitivity (d_{10}) of the target microbes.

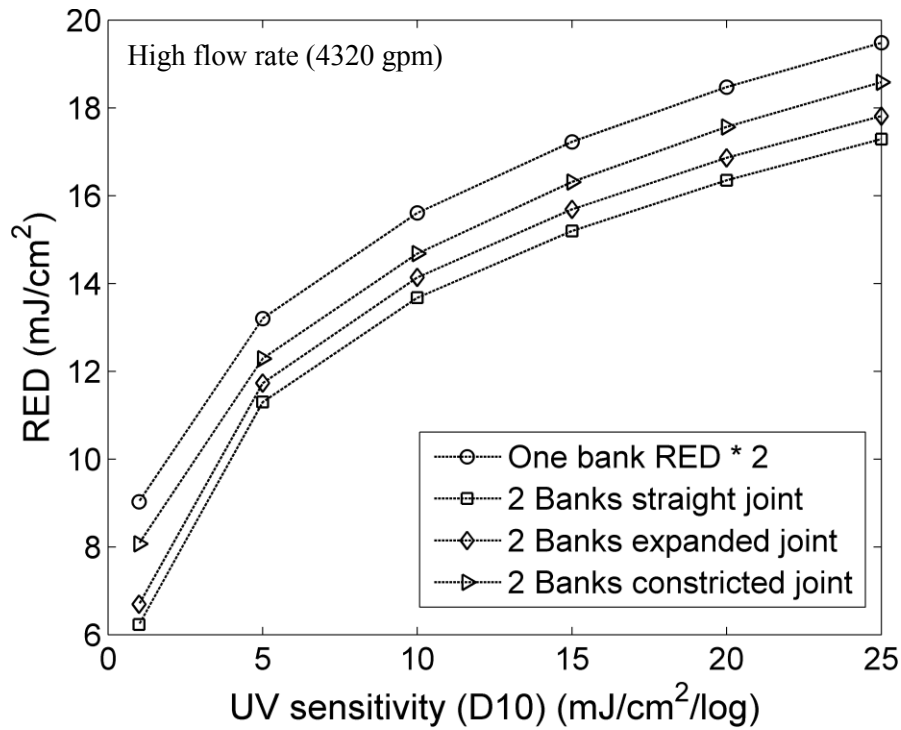


Figure 4.25 Reduction equivalent dose (RED) for the two-bank reactors compared with the one-bank reactor at 4320 gpm.

Table 4.1 Additive behavior of RED in the reactors with two lamp banks

| d10 values $\left[\frac{mJ}{cm^2 \log} \right]$ | Reactor with only one bank RED $\left[\frac{mJ}{cm^2} \right]$ | Reactor with two lamp banks in series (4320 gpm) | | | | | |
|---|---|--|--------|----------------|--------|-------------------|--------|
| | | Straight joint | | Expanded joint | | Constricted joint | |
| | | RED | M. F. | RED | M. F. | RED | M. F. |
| 1 | 4.5151 | 6.2338 | 1.3807 | 6.6952 | 1.4828 | 8.0689 | 1.7871 |
| 5 | 6.6017 | 11.2972 | 1.7113 | 11.7298 | 1.7768 | 12.2885 | 1.8614 |
| 10 | 7.8028 | 13.6737 | 1.7524 | 14.1370 | 1.8118 | 14.6808 | 1.8815 |
| 15 | 8.6141 | 15.1963 | 1.7641 | 15.6882 | 1.8212 | 16.3122 | 1.8937 |
| 20 | 9.2363 | 16.3511 | 1.7703 | 16.8622 | 1.8257 | 17.5671 | 1.9020 |
| 25 | 9.7408 | 17.2874 | 1.7747 | 17.8104 | 1.8284 | 18.5860 | 1.9081 |

4.8 Scaled Down Reactor

In the following section, the hydrodynamic and disinfection behaviors of the scaled down model are compared with the full size one. The comparison elucidates the applicability of the developed scaling down methodology.

4.8.1 Hydrodynamic Behaviour of the Scaled Down Reactor

The free surface height for the scaled down reactor is compared with that of the full size reactor as shown in Figure 4.26. For the sake of comparison, in this figure the free surface height from the scaled down system is multiplied by the scaling ratio. It can be noticed that for the same Froude number, the free surface profile for the small scale reactor has similar fluctuation as the full size one. However, the amplitude of the surface waviness is somewhat reduced. This deviation could be due to the reduction of Reynolds number by one order of magnitude, while keeping the Froude number the same. Probably the increase in the viscous forces might have attenuated the surface fluctuations through viscous damping.

It can be observed that for the scaled down reactor, maintaining both the Froude and Reynolds numbers the same between the model and full size reactors, shows almost similar free surface shape, with a slight deviation at the downstream of the lamps.

Figure 4.27 shows that, for the reactor under consideration, the residence time has a narrow distribution suggesting that the use of mean velocity ratio to calculate the residence time ratio is not that erroneous.

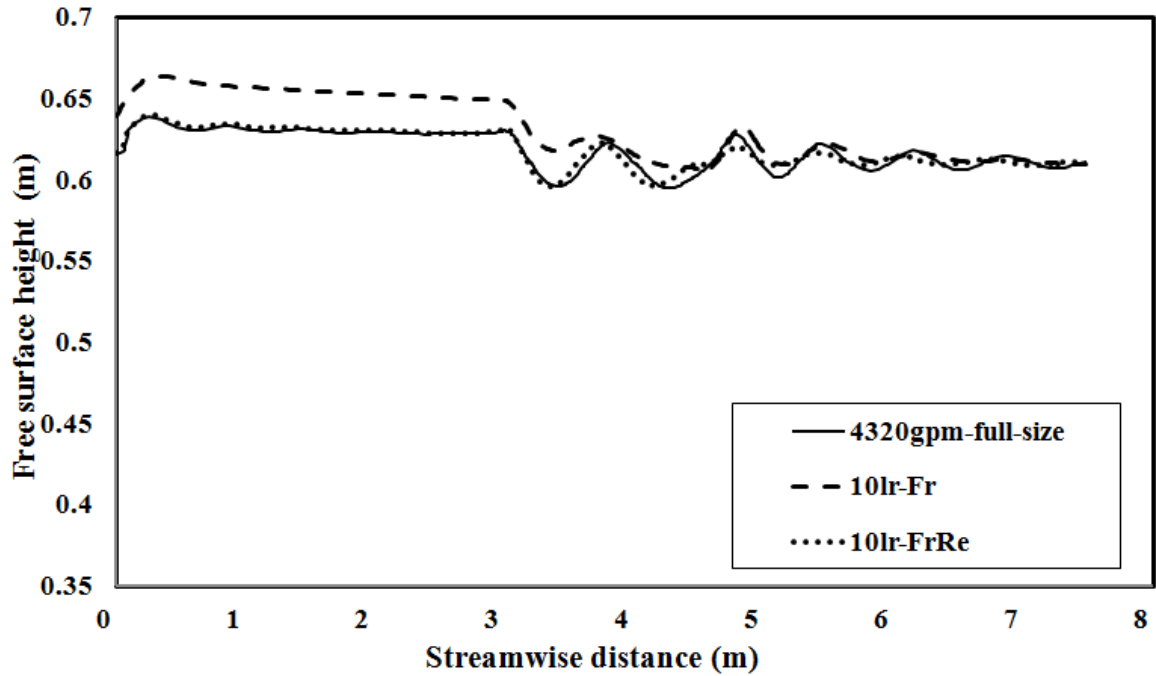


Figure 4.26 Comparison of free surface profile for the full size and scaled down systems

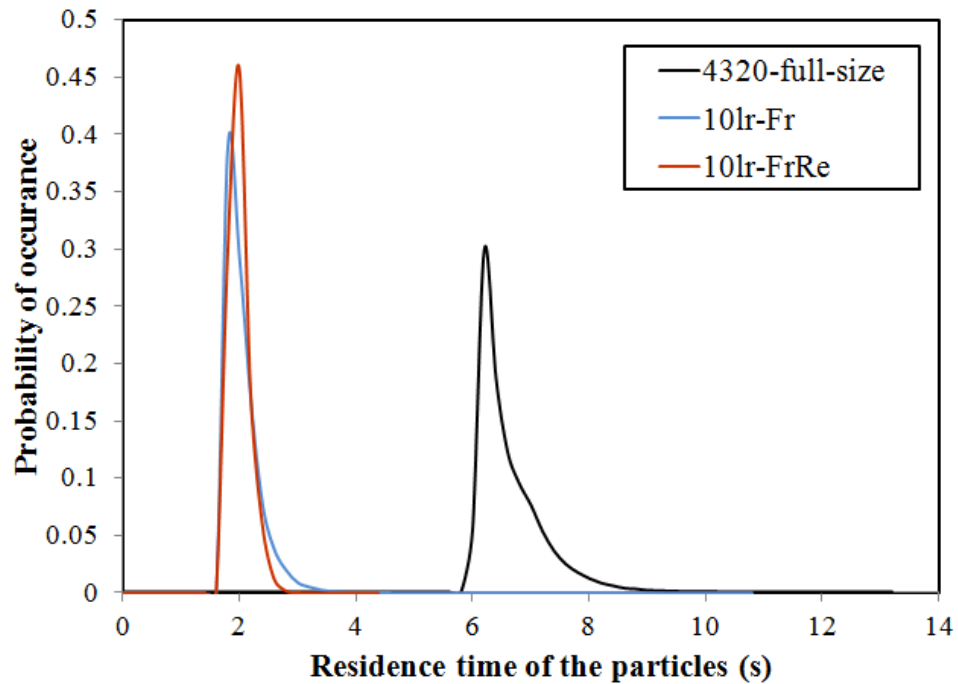


Figure 4.27 Probability density of particle residence time at full size and scaled down models.

4.8.2 Disinfection Behaviour of the Scaled Down Reactor

Figure 4.28 shows the disinfection characteristics of the full size and the small scale reactors. The achievable log removal values for the small scale reactor agree better with the full size reactor when using both Reynolds and Froude numbers compared to the one using the Froude number only. The deviation in log removal values especially in the low d_{10} region can be attributed to the deviation in the free surface shape in scaled down model using only Froude number. This error can however be mitigated by ensuring that the volume averaged intensity value is scaled down.

Figure 4.29 shows that the average dose and the dose distribution both remains the same as per the requirements set to maintain the same log removal and consequently the RED of the reactor. However, for reactor scaled with the Froude number only, the distribution is slightly wider thus affecting the log removal in the low d_{10} region.

The above results suggest that the scaling down methodology works reasonably well. Keeping only the Froude number constant, along with implementing the developed scaling down procedure in radiation field can produce nearly similar disinfection behavior. If both the Froude and Reynolds number are kept constant, the scaled down reactor produces exactly same disinfection behavior. However, the implementation of this technique in the experiments requires the decrease in viscosity value of the working fluid. The viscosity modifier additives available in the commercial market can be used for that purpose.

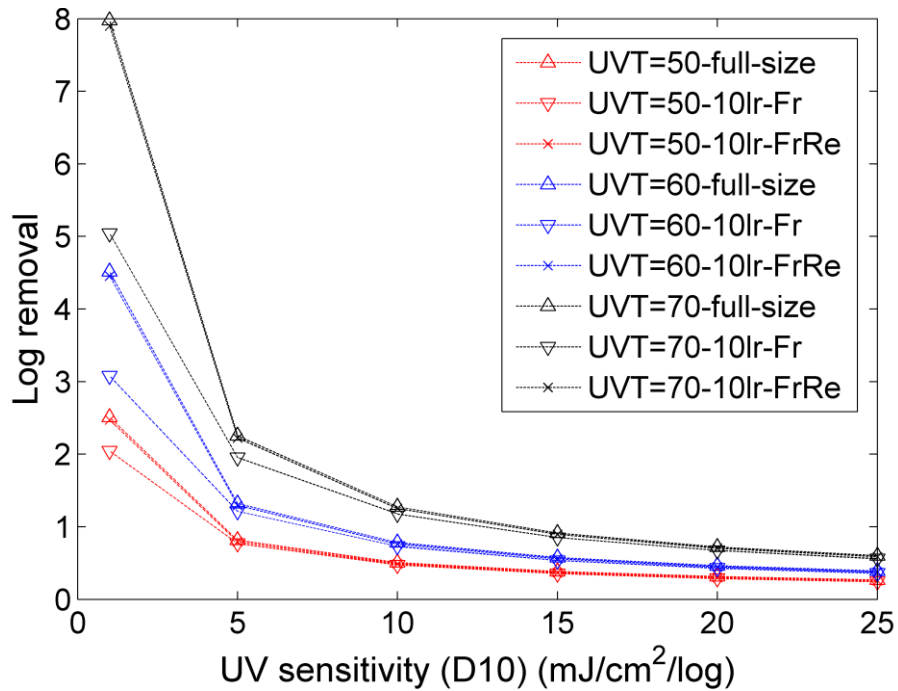


Figure 4.28 Comparison of the disinfection performance between the full size (4320 gpm) and scaled down models using only the Froude number and both Reynolds & Froude numbers

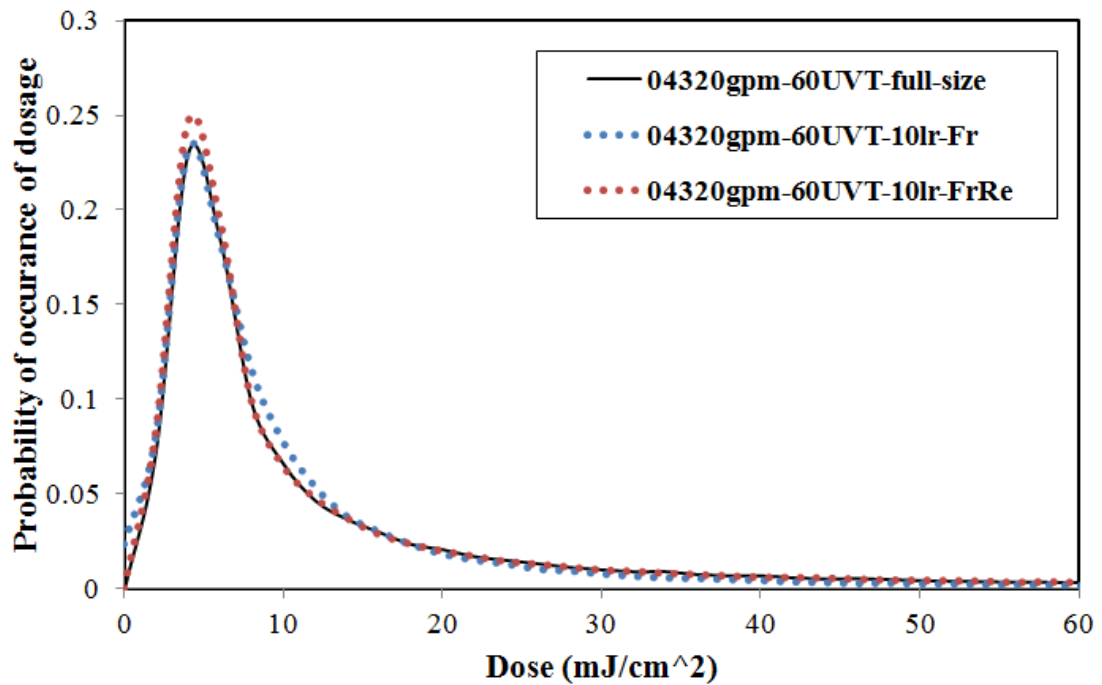


Figure 4.29 Probability density of dosage at the full size and scaled down reactors.

Chapter 5

5 Conclusions

A comprehensive CFD model was developed to study the performance of an open channel ultra-violet wastewater disinfection reactor. The developed model was validated against the available experimental data. It was found that the multiphase volume of fluid (VOF) method along with the selected turbulence models can well describe the physics of the open channel flow. Both the Reynolds stress model and the realizable $k - \epsilon$ model predicted similar turbulence characteristics. Since no secondary fluid motion was observed, suggesting the effect of anisotropy in turbulence is negligible for this reactor, the realizable $k - \epsilon$ model can be used for further studies considering its lower computational cost.

A parametric study was performed to investigate the influence of different parameters on the performance of the open channel reactor. It was evident that the decrease in the flow velocity would improve the disinfection performance. The developed CFD model can quantify the extent of the improvement. It was noticed that a velocity boundary layer is formed around the lamps which becomes thicker at lower flow velocity. This boundary layer development inhibits proper lateral mixing. Therefore, modification to the reactor geometry such as addition of baffles could be considered.

It was observed that the shape of the free surface especially in the lamp region affects the disinfection performance of the reactor. Therefore, the rigid lid approximation at the free surface is not recommended. It was identified that, for microbes having very low UV sensitivity, the disinfection performance gets very little improvement if the water UV transmittance (UVT) is increased. This suggests that, to improve the inactivation of the low UV sensitive microbes, rather than improving the water UVT, other methods need to be considered. For example, the distance between the lamps could be decreased or some filler rods could be inserted in the regions away from the lamps where UV intensity is low.

Effective visualization technique was developed which could be utilized to plot the low dosed particles within the reactor. This method could be useful in the decision making during the reactor design process to improve its dose distribution.

It was found that for all the reactors having two lamp banks the achievable reduction equivalent dose (RED) is lower than twice of the RED of a reactor having only one bank. The reactor having a constricted joint between the two lamp banks exhibited the highest positive influence on the additive nature of the disinfection. The reactor having expanded joint exhibited comparatively better disinfection behavior than the one having straight joint. These findings suggest that, while placing the lamp banks in series, both the constricted and expanded joint could be considered to improve the overall disinfection performance.

The scalability of the open channel ultra-violet disinfection reactor was also investigated. Scaling methodology for the hydraulics and optics were developed from the theoretical and practical considerations. Two scaling methods were evaluated: 1) the Froude number was kept constant and 2) both the Froude and the Reynolds numbers were kept constant by modifying the viscosity of the working fluid. Scaling methodology for the UV radiation field was formulated to ensure the same RED values for the full size and scaled down reactors. This methodology was implemented numerically using the developed CFD model. The full size and the scaled down reactors exhibited similar hydraulic and disinfection characteristics. For highly UV sensitive microbes some deviations in the achieved log removal were observed when only the Froude number was kept constant. However, when both the Froude and Reynolds numbers were kept constant, the scaled down reactor produced the same disinfection behavior. Therefore, experiments could be performed following this scaling down methodology to further validate the procedure. If validated, the behavior of a large scale open channel disinfection reactor could be predicted from a small scale laboratory test.

References

- Abbaspour, A., D. Farsadizadeh, A. H. Dalir, and A. A. sadraddini (2009). Numerical study of hydraulic jumps on corrugated beds using turbulence models. *Turkish Journal of Engineering and Environmental Sciences* 33, 61–72.
- Akoz, M. S., M. S. Kirkgoz, and A. A. Oner (2009). Experimental and numerical modeling of a sluice gate flow. *Journal of Hydraulic Research* 47(2), 167–176.
- ANSYS FLUENT Theory Guide (2010, November). release 13. Ansys Inc.
- Asano, T. (2007). *Water reuse : issues, technology, and applications*. McGraw-Hill, New York.
- Blatchley, E., C. Shen, Z. Naunovic, L. Lin, D. Lyn, J. Robinson, K. Ragheb, G. Gregori, D. Bergstrom, S. Fang, Y. Guan, K. Jennings, and N. Gunaratna (2006). Dyed microspheres for quantification of UV dose distributions: Photochemical reactor characterization by Lagrangian actinometry. *Journal of Environmental Engineering* 132(11), 1390–1403.
- Bohrerova, Z., G. Bohrer, S. Mohanraj, J. Ducoste, and K. Linden (2005, November 15). Experimental measurements of fluence distribution in a UV reactor. *Environment Science and Technology* 39(22), 8925–8930.
- Bolton, J. R. (2000). Calculation of ultraviolet fluence rate distributions in an annular reactor: significance of refraction and reflection. *Water Research* 34(13), 3315 – 3324.
- Cabaj, A. and R. Sommer (2000). Measurement of ultraviolet radiation with biological dosimeters. *Radiation Protection Dosimetry* 91(1-3), 139–142.
- Cassan, L. and G. Belaud (2012). Experimental and numerical investigation of flow under sluice gates. *Journal of Hydraulic Engineering* 138(4), 367–373.

Cea, L., L. Pena, J. Puertas, M. E. Vázquez-Cendón, and E. Peña (2007). Application of several depth-averaged turbulence models to simulate flow in vertical slot fishways. *Journal of Hydraulic Engineering* 133(2), 160–172.

Chevrefils, G., Éric Caron, H. Wright, G. S. and Pierre Payment, B. Barbeau, and B. Cairn (IUVA news 2006, March). UV dose required to achieve incremental log inactivation of bacteria, protozoa and viruses.

Chiu, K., D. Lyn, P. Savoye, and E. Blatchley III (1999a). Integrated UV disinfection model based on particle tracking. *Journal of Environmental Engineering* 125(1), 7–16.

Chiu, K., D. Lyn, P. Savoye, and E. Blatchley III (1999b). Effect of UV system modifications on disinfection performance. *Journal of Environmental Engineering* 125(5), 459–469.

Demuren, A. O. and W. Rodi (1984). Calculation of turbulence-driven secondary motion in non-circular ducts. *Journal of Fluid Mechanics* 140, 189–222.

Downey, D., D. Giles, and M. Delwiche (1998). Finite element analysis of particle and liquid flow through an ultraviolet reactor. *Computers and Electronics in Agriculture* 21(2), 81 – 105.

Ducoste, J., D. Liu, and K. Linden (2005). Alternative approaches to modeling fluence distribution and microbial inactivation in ultraviolet reactors: Lagrangian versus Eulerian. *Journal of Environmental Engineering* 131(10), 1393–1403.

Elyasi, S. and F. Taghipour (2006). Simulation of UV photoreactor for water disinfection in Eulerian framework. *Chemical Engineering Science* 61(14), 4741 – 4749.

Elyasi, S. and F. Taghipour (2011). Performance evaluation of UV reactor using optical diagnostic techniques. *AIChE Journal* 57(1), 208–217.

Gandhi, V. N., P. J. W. Roberts, and J.-H. Kim (2012). Visualizing and quantifying dose distribution in a UV reactor using three-dimensional laser-induced fluorescence. *Environmental Science & Technology* 46(24), 13220–13226.

Jha, S. and F. Bombardelli (2009). Two-phase modeling of turbulence in dilute sediment-laden, open-channel flows. *Environmental Fluid Mechanics* 9, 237–266. 10.1007/s10652-008-9118-z.

Jing, H., Y. Guo, C. Li, and J. Zhang (2009). Three-dimensional numerical simulation of compound meandering open channel flow by the reynolds stress model. *International Journal for Numerical Methods in Fluids* 59(8), 927–943.

Kang, H. and S.-U. Choi (2006). Reynolds stress modelling of rectangular open-channel flow. *International Journal for Numerical Methods in Fluids* 51(11), 1319–1334.

Linden, K., G. Shin, and M. Sobsey (2001). Comparative effectiveness of UV wavelengths for the inactivation of *Cryptosporidium Parvum* oocysts in water. *Water Sci Technol* 43(12), 171–174.

Linden, K. G., G.-A. Shin, G. Faubert, W. Cairns, and M. D. Sobsey (2002). UV disinfection of *Giardia lamblia* cysts in water. *Environmental Science & Technology* 36(11), 2519–2522.

Liu, D. (2004). *Numerical simulation of UV disinfection reactors: impact of fluence rate distribution and turbulence modeling*. Ph. D. thesis, Department of Civil, Construction, and Environmental Engineering, North Carolina State University.

Liu, D., J. Ducoste, S. Jin, and K. Linden (2004). Evaluation of alternative fluence rate distribution models. *Journal of Water Supply: Research & Technology-AQUA* 53(6), 391 – 408.

Liu, D., C. Wu, K. Linden, and J. Ducoste (2007). Numerical simulation of UV disinfection reactors: Evaluation of alternative turbulence models. *Applied Mathematical Modelling* 31(9), 1753 – 1769.

Lyn, D. (2004). Steady and unsteady simulations of turbulent flow and transport in ultraviolet disinfection channels. *Journal of Hydraulic Engineering* 130(8), 762–770.

Lyn, D. and E. Blatchley (2005). Numerical computational fluid dynamics-based models of ultraviolet disinfection channels. *Journal of Environmental Engineering* 131(6), 838–849.

Lyn, D., K. Chiu, and E. Blatchley III (1999). Numerical modeling of flow and disinfection in UV disinfection channels. *Journal of Environmental Engineering* 125(1), 17–26.

Ma, L., P. J. Ashworth, J. L. Best, L. Elliott, D. B. Ingham, and L. J. Whitcombe (2002, 5/1). Computational fluid dynamics and the physical modelling of an upland urban river. *Geomorphology* 44(34), 375–391.

Ming-Hsi, H., C. Chun-Hung, and T. Wei-Hsien (2001). An arbitrary Lagrangian-Eulerian finite difference method for computations of free surface flows. *Journal of Hydraulic Research* 39(5).

Morsi, S. A. and S. A. Alexander (1972, September 26). An investigation of particle trajectories in two phase flow systems. *Journal of Fluid Mechanics* 55(2), 193–208.

Munoz, A., S. Craik, and S. Kresta (2007). Computational fluid dynamics for predicting performance of ultraviolet disinfection - sensitivity to particle tracking inputs. *Journal of Environmental Engineering and Science* 6(3), 285–301.

Nezu, I. and H. Nakagawa (1984). Cellular secondary currents in straight conduit. *Journal of Hydraulic Engineering* 110(2), 173–193.

Nezu, I., H. Nakagawa, and W. Rodi (1989). Significance difference between secondary currents in closed channels and narrow open channels. In *Proceedings of 23rd IAHR Congress*, Volume A, Delft, The Netherlands, pp. 125–132.

Nezu, I. and M. Sanjou (2006). Numerical calculation of turbulence structure in depth-varying unsteady open-channel flows. *Journal of Hydraulic Engineering* 132(7), 681–695.

Nezu, I., A. Tominaga, and H. Nakagawa (1993). Field measurements of secondary currents in straight rivers. *Journal of Hydraulic Engineering* 119(5), 598–614.

Oppenheimer, J. A., J. G. Jacangelo, J.-M. Laine, and J. E. Hoagland (1997). Testing the equivalency of ultraviolet light and chlorine for disinfection of wastewater to reclamation standards. *Water Environment Research* 69(1), pp. 14–24.

Pan, H. and M. Orava (2007). Performance evaluation of the UV disinfection reactors by CFD and fluence simulations using a concept of disinfection efficiency. *Journal of Water Supply: Research and Technology - AQUA* 56(3), 181–189.

Patil, S., M. Kostic, and P. Majumder (2009). Computational fluid dynamics simulation of open-channel flows over bridge-decks under various flooding conditions. In *6th WSEAS International Conference on FLUID MECHANICS (FLUIDS'09)*.

Peng, B., D. Santoro, M. Sasges, B. Petri, and D. Olson (2012, 25-29 November). Free surface effects and UV disinfection in open channel UV reactors. México City, Mexico. International Water Association Conference.

Rameshwaran, P. and P. Naden (2003). Three-dimensional numerical simulation of compound channel flows. *Journal of Hydraulic Engineering* 129(8), 645–652.

Sinha, S. K., F. Sotiropoulos, and A. J. Odgaard (1998). Three-dimensional numerical model for flow through natural rivers. *Journal of Hydraulic Engineering* 124(1), 13–24.

Smolentsev, S., M. Abdou, N. Morley, A. Ying, and T. Kunugi (2002). Application of the k- ϵ model to open channel flows in a magnetic field. *International Journal of Engineering Science* 40(6), 693 – 711.

Sozzi, D. A. and F. Taghipour (2006). UV reactor performance modeling by Eulerian and Lagrangian methods. *Environmental Science & Technology* 40(5), 1609–1615. PMID: 16568777.

Srinivas, C. (1992, August). Two dimensional modelling of flow and sedimentation. Master's thesis, Rice University.

Sugiyama, H., D. Hitomi, and T. Saito (2006). Numerical analysis of turbulent structure in compound meandering open channel by algebraic Reynolds stress model. *International Journal for Numerical Methods in Fluids* 51(7), 791–818.

USEPA (2006, November). *Ultraviolet disinfection guidance manual for the final long term 2 enhanced surface water treatment rule*. 1200 Pennsylvania Avenue NW. Washington, DC 20460-0001: United States Environmental Protection Agency, Office of Water.

Wols, B., L. Shao, W. Uijtewaal, J. Hofman, L. Rietveld, and J. van Dijk (2010). Evaluation of experimental techniques to validate numerical computations of the hydraulics inside a UV bench-scale reactor. *Chemical Engineering Science* 65(15), 4491 – 4502.

Wright, H. B. and W. L. Cairns (1998, October 27-29). Ultraviolet light. In *Regional Symposium on Water Quality: Effective Disinfection*, Lima, Peru. CEPIS, Pan-American Centre of Sanitary Engineering and Environmental Sciences.

Wright, N. and D. Hargreaves (2001). The use of CFD in the evaluation of UV treatment systems. *Journal of Hydroinformatics* 3, 59–70.

Wu, W., W. Rodi, and T. Wenka (2000). 3d numerical modeling of flow and sediment transport in open channels. *Journal of Hydraulic Engineering* 126(1), 4–15.

Younis, B. A. and T. H. Yang (2010). Computational modeling of ultraviolet disinfection. *Water Science & Technology* 62(8), 1872–1878.

Younis, B. A. and T. H. Yang (2011). Prediction of the effects of vortex shedding on UV disinfection efficiency. *Journal of Water Supply: Research & Technology-AQUA* 60(3), 147 – 158.

Appendices

Appendix A - User Defined Function (UDF)

The skeleton of this UDF was found from the Sandia National Laboratories website. It was updated to suit the open channel flow application and new features were added.

```

/*****
/* Compiled UDF for integrating the UV intensity over time along a particle */
/* trajectory. Particles are deleted from the domain if it reaches a cell where */
/* volume fraction is very small. Low dosed particles are identified and */
/* residence times are obtained at the reactor outlet. */
*****/
#include "udf.h"
#include "dpm.h"
#include "sg_disco.h" /* to access the UV intensity values at the cell */
#define C_DO(c,t)C_STORAGE_R_XV(c,t,SV_DO_IRRAD,0)

#define fdout "doseout.txt"
#define ftrack "trackfilters.txt"
#define ftime "restime.txt"
FILE *pdout;
FILE *ptrack;
FILE *ptime;

static real uv_intensity;

/* Macro for integrating the UV intensity over time along a particle trajectory */
DEFINE_DPM_SCALAR_UPDATE(uv_dosage, cell, thread, initialize, p)
{
    cphase_state_t *c = &(p->cphase);
    Thread *ts=THREAD_SUB_THREAD(thread,1); /* get the water domain thread */

    if (initialize)
    {
        {
            p->user[0] = 0.;
            uv_intensity = C_DO(cell,thread);
        }
    }
    else
    {
        {
            if(C_VOF(cell,ts)<0.001)
            {
                /* particle deleted if it reaches a cell where water VF is <0.001 */
                p->stream_index=-1;
            }
            else
            {
                /* UV intensity integrated over time using Trapezoidal rule */
                p->user[0] += P_DT(p) * .5 * (uv_intensity + C_DO(cell,thread));
                uv_intensity = C_DO(cell,thread);
            }
        }
    }
}

```

```

    }
  }
}

/* Macro for writing the UV dosage, residence time and the ID for low dosed */
/* particles at reactor outlet. */

DEFINE_DPM_OUTPUT(uv_output, header, fp, p, thread, plane)
{
  if (header)
  {
  }
  else
  {
    /* write the dosage values */
    pdout=fopen(fdout,"a"); /* delete previous files */
    fprintf(pdout,"%10.6g \n",p->user[0]);
    fclose(pdout);

    /* write the particle id of low dosed particles */
    ptrack=fopen(ftrack,"a"); /* delete previous files */
    if(p->user[0]<30.0) /* change this value accordingly */
    {
      fprintf(ptrack,"%d,",p->part_id);
    }
    fclose(ptrack);

    /* write the particle residence times */
    ptime=fopen(ftime,"a"); /* delete previous files */
    fprintf(ptime,"%10.6g \n",p->state.time);
    fclose(ptime);
  }
}

```

Curriculum Vitae

Name: Rajib Kumar Saha

Post-secondary Education and Degrees: The University of Western Ontario
London, Ontario, Canada
2011-2013 M.E.Sc. in Mechanical & Materials Engineering

Bangladesh University of Engineering and Technology
Dhaka, Bangladesh
2009-2011 M.Sc. in Mechanical Engineering

Bangladesh University of Engineering and Technology
Dhaka, Bangladesh
2004-2009 B.Sc. in Mechanical Engineering

Honours and Awards: Western Graduate Research Scholarship
2011-2013

Technical Scholarship, Bangladesh Government
2004-2008

Related Work Experience Teaching Assistant
Dept. of MME, The University of Western Ontario
2011-2013

Graduate Research Assistant
Dept. of MME, The University of Western Ontario
2011-2013 (Summer)